ON USING THE UPPER TRIANGULAR (QR) DECOMPOSITION THEOREM FOR DERIVING A NEW STRAIN ENERGY FUNCTION FOR THE INCOMPRESSIBLE AND ORTHOTROPIC PASSIVE MYOCARDIUM

A Thesis

by

TAWFIK MOHAMMED HUSSEIN

Submitted to the Office of Graduate and Professional Studies of
Texas A&M University
in partial fulfillment of the requirements for the degree of

MASTER OF SCIENCE

Chair of Committee,	John C. Criscione
Committee Members,	Saurabh Biswas
	Nicholas B. Suntzeff
Head of Department,	Michael J. McShane

August 2020

Major Subject: Biomedical Engineering

ABSTRACT

Developing models describing myocardial deformation have been central to understanding cardiac function, both normal and abnormal. However, the widely used Fung model is known to have high degeneracy and thus less unique solutions. Therefore, the goal of this work was to derive a strain energy function for the incompressible myocardium with less degeneracy and more uniqueness than the Fung model. The upper triangular (QR) decomposition theorem was leveraged to develop a model that achieved the stated goal. Furthermore, published biaxial data was utilized from studies that measure the stresses of slabs of myocardium to find the respective functional form for the strain energy function using the QR model as well as estimate the resulting material stiffness constants. The respective model was then compared with the strain energy function obtained from the Fung model. The outcome of this work was a model that improves on the Fung model in having fewer constraints and degeneracy that results in a reduction of the uncertainty and enhances the predictability for the mechanical behavior of the heart.

DEDICATION

I dedicate this work to all those who suffer from heart disease and to future scholars who will pursue this work and carry on the benefit to all mankind.

ACKNOWLEDGEMENTS

This thesis was completed in 2020, a year that challenged the country and the world with the COVID-19 pandemic and a calling for social change. First and foremost, I would like to thank my advisor and mentor, Prof. John Criscione, for inspiring me and sparking my interest to pursue the challenging and exciting field of cardiac mechanics. His door was always open for me, and my understanding and appreciation for the heart would not be where it is today without his great insight, guidance, and support.

Second, I would like to thank Dr. Biswas for his great insights in entrepreneurship, and for providing me with an interesting project to work on related to cardiac twist and its use in diagnostics. I also would like to thank Prof. Suntzeff for igniting my appreciation for the wonders of the universe. Our extended "office hour" discussions at Starbucks were some of the best I had during my time at Texas A&M. These discussions have made the similarity between the heart and the cosmos all the more clear to me.

I also would like to thank my academic advisors, Jake Clough and Mrs. Stormy Kretzschmar for helping me navigate the logistical loops. Thanks also go to my second family in the LAUNCH office, especially the UGR glam squad, and all my friends in the BMEN department for making my time at Texas A&M a great experience.

Finally, I owe a great debt of gratitude to my dear parents, for their tremendous support and encouragement. I would not be where I am today without them.

CONTRIBUTORS AND FUNDING SOURCES

Contributors

This work was supervised by a thesis committee consisting of Prof. John C. Criscione and Dr. Saurabh Biswas of the Department of Biomedical Engineering and Prof. Nicholas B. Suntzeff of the Department of Physics and Astronomy.

All the work conducted for the thesis was completed by the student independently.

Funding Sources

Graduate study did not receive any funding for the completion of the work.

NOMENCLATURE

$\mathbf{A}_i$	Deviatoric Basis Tensor
$\mathbf{C}$	Right Cauchy-Green Stretch Tensor
$\mathbf{E}$	Green Strain Tensor
$\mathbf{F}$	Deformation Gradient Tensor
$\mathbf{f}$	Upper Triangular Stretch Tensor
$\mathbf{I}$	Identity Tensor
J	Jacobian
$\mathbf{L}$	Deviatoric Kinematic Tensor
p	Pressure-like Lagrange Multiplier
$\mathbf{Q}$	Pure Rotation Tensor
Q	Material Function of Stiffness
$\mathbf{R}$	Rotation Tensor
$\mathbf{U}$	Right Stretch Tensor
$\mathbf{V}$	Left Stretch Tensor
W	Strain Energy Function
α_i	Strain Parameter (Attribute)
λ_i	Stretch Mode of Deformation
ϕ_{ij}	Shear Mode of Deformation
$\boldsymbol{\sigma}$	Cauchy (True) Stress

TABLE OF CONTENTS

Page

LIST OF FIGURES

Page

LIST OF TABLES

Page

CHAPTER I

INTRODUCTION

1.1 Background

Biomechanics is defined as the development, extension, and application of mechanics—the study of force and motion—to understanding biological systems (Humphrey 2003). The endeavor to understand the behavior of biological tissues through the lens of mechanics dated back to the 16th century, when Leonardo da Vinci studied the flight of birds in an attempt to replicate the process for humans (Humphrey 2003). Galileo then followed by studying the mechanical strength of bones to understand the role of the skeletal system in the stability of large mammals (Humphrey 2003). Furthermore, Malpighi, Borelli, and Descartes were key figures, who went on to establish the iatrophysical approach to medicine, which held that the mechanics rather than the chemistry was the key to understanding the function of the human body (Martin 1999). Hence, this work and others in the field of biomechanics are motivated either directly or indirectly by this notion, given how intertwined the mechanics is with the biological behavior of tissues.

Biomechanics lies at the heart of formulating a solid foundation for understanding human medicine. Furthermore, mechanics is central to understanding the human body across all levels, from the behavior of quarks in atomic nuclei to full organ systems. The behavior of soft tissues, defined as materials that undergo “large” deformations, is no exception; that is, large relative to conventional engineering materials such as metals,

alloys, concrete, and wood, which obey the classical linear theory of elasticity and fall within the range of applicability of Hooke's Law (Fung 1967). Furthermore, the maximum strain a metal can undergo is 0.2% whereas soft tissues can undergo strains that far exceed that. To illustrate, **Table 1** represents the extent of strain certain soft tissues can undergo (Fung 1967).

Table 1. The extent of strain for various types of human soft tissue. Adapted from (Fung 1967)

	Maximum Strain
Papillary Muscles	5%
Skin	10% – 40%
Blood Vessels	30% – 70%
Mesentery	100%
Isolated Striated Muscle Fibers	140%

As a result, the behavior exhibited by soft tissues—particularly how stress depends on the motion—is nonlinear, heterogeneous, inelastic, and anisotropic. The behavior of the heart is no exception.

1.2 The "Proper" Theoretical Framework for Cardiac Mechanics

To understand the mechanics of the heart, one must first establish the "appropriate" level of understanding that is sought after in this work. There are five main levels to mechanics, each level exploiting a different level of matter (Humphrey 2002). These levels can be illustrated through a simple thought experiment that involves a conventional tennis

ball contacting a racket during a serve. As the tennis ball collides with the strings of the racket, the shape of the tennis ball before and after the collision is spherical. Hence, if the analysis of interest pertains to the impact of the external forces (such as collision and air drag) on the behavior of the tennis ball as a whole, then assuming the tennis ball as a discrete particle at its center of mass is sufficient for conducting the analysis. This first level is discrete mechanics, which describes the mechanics of objects as rigid bodies.

However, if one were to consider the instant it collides with the strings of the tennis racket, the mechanics would differ. At that moment, because the hollow rubber core of the tennis ball is a compliant material and contains pressurized air, the tennis ball will deform momentarily. To understand the mechanics of the finite subregions within the tennis ball, a simple look at the external forces is insufficient as there are now forces "within" the tennis ball that developed as a result of the deforming collision. Hence, this second level describing the impact of the forces within the material on the behavior of the material (i.e., how it depends on the deformation) is known as continuum mechanics.

Let us "freeze" the snapshot of the impacted tennis ball and magnify the site of contact between the ball and the strings sufficiently enough to see the cluster of atoms. What will be observed is the atoms vibrating in a "jiggling" motion, and due to the elasticity of the impacted strings, energy will be generated within the strings in the form of increased strain potential energy partly converted to heat, that is thermal motion of the atoms and molecules. This forces the cluster to occupy a higher energy state. Hence, the impact will increase the entropy of the atoms of the strings causing this "molecular cluster" comprising the strings to return to the lower energy state it once occupied. Therefore,

understanding how matter behaves on the scale of atomic clusters and observing the energy dispersion impacting the molecular degrees of freedom are described by statistical mechanics, the third level of mechanics.

As this snapshot is magnified further to observe an individual atom, it will become apparent that the majority of this realm is empty space with a dense cluster of particles (i.e., nucleus) in its center and negatively charged particles that lie in a probability distribution around that dense cluster (i.e., electrons). Even so, it is rather difficult to quite "see" these electrons as they rather form clouds around the nucleus, which makes determining their location in space a game of probability. This fourth level is known as quantum mechanics, which describes the behavior of matter on atomic and subatomic scales.

The fifth and final level is a rather overarching level that impacts the previous four levels. If the interaction between the tennis ball and the racket took place on a spaceship rather than Earth, traveling at a speed that is a significant fraction of the speed of light, then new considerations must be factored in as the tennis ball will experience, as a result, profound effects such as a contraction in its length and dilation of its mass and time relative to an observer on Earth. Such effects are known as relativistic effects, which result from objects moving at high speeds (i.e., approaching that of the speed of light) or being within close proximity of a high gravitational source (such as orbiting a black hole) that create significant distortions in the space-time continuum. This level is known as relativistic mechanics.

Hence, it is crucial to determine the appropriate level of mechanics that provides a sound theoretical framework that is deemed "appropriate" for the analysis of the mechanics of the heart. Furthermore, because the interest is in the behavior of the heart with the surface of the Earth as the global reference frame, no relativistic effects need be taken into consideration. Additionally, this works seeks to analyze the behavior of the heart on the scale of the myocardial tissue, particularly how the stress within depends on its deformation, where the finite subregions of the myocardium behave as the aggregate, the myocardium, behaves (Criscione 2011). Therefore, to observe such deformations, the external forces must be isolated, implying that the body needs to be static, rendering discrete mechanics insufficient. Additionally, the scale is relatively large for statistical and quantum mechanics to be the framework of choice, and neither the change in entropy nor energy is the primary focus of this work. Therefore, cardiac soft tissue mechanics is conducted within the framework of continuum mechanics, the overarching framework of this thesis.

1.3 Constitutive Models

With continuum mechanics established as the overarching theoretical framework of this thesis, there are various concepts essential to consider when solving problems in the field of continuum mechanics (Humphrey 2002). Such concepts are the concept of kinematics, the concept of force, balance equations, and constitutive models (Humphrey 2002). While the former three are quite established, the latter fourth is always in need of improvement, especially for that of the heart, the focus of this thesis. Constitutive relations

can be defined as the descriptions of the response of a material to applied loads (which depends on the internal constitution of the material) under the conditions of interest (Humphrey 2002). There is a great need for "good" models that provide predictive capabilities that facilitate modeling diseases and innovating sounder therapeutic interventions. Furthermore, such models allow for a sounder understanding of the behavior of the myocardium and the associated parameters that control such behavior.

Developing a constitutive model for the heart (or any soft tissue for that matter) is no trivial task. It should, furthermore, be understood that heart is a "real thing", and real things are ananalytical. That is, no models exist that are "perfect" with exact solutions. However, with a certain degree of uncertainty, certain approximations can be made to obtain a model that is "acceptable", that lies within an accepted degree of uncertainty and that is deemed "appropriate" for the intended application. There are two methods to obtain such solutions for "real" problems, the analytical approach known as perturbation theory, and the experimental approach known as numerical methods, which is semi-empirical. The widely used method in the field of cardiac mechanics is finding the numerical solution from experiments. Hence, the numerical approach will be the method adopted in this thesis.

1.4 Cardiac Deformation and Its Centrality to Its Function

To gain a better grasp of how essential deformation is for the physiology of the heart, one must first define what deformation is and then relate it to the function of the heart. Deformation can be simply defined as a process of dilatation and distortion of a

material. Furthermore, dilatation is defined as a change in size whereas distortion is defined as a change in shape. There are two types of distortion that are relevant to cardiac deformation, which are pure shear (i.e., stretching the faces) and simple shear (i.e., stretching along the diagonals) as demonstrated in the following figures (**Figures 1, 2**).

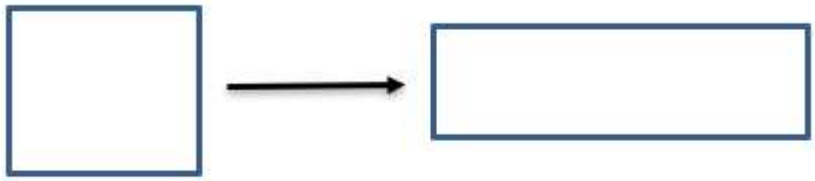

Figure 1. Pure shear of a two-dimensional plane along the horizontal axis

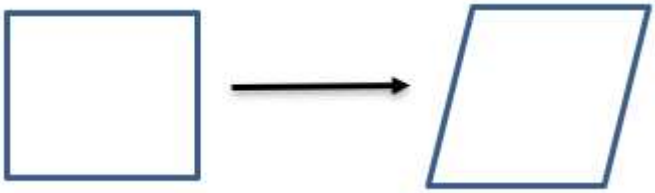

Figure 2. Simple shear of a two-dimensional plane along the horizontal axis

To put these concepts in a mechanical perspective, dilatation is measured as stretch, which is found from dividing the current length of an object to its initial length; in addition, distortion can be quantified from shear. Both dilatation and distortion are modes of motion for a deformable body in addition to that of the rigid bodies, which are translation, and rotation. Therefore, the mechanical motion of the heart can be quantified from the stretch and shear of its fibers in various directions.

Because the ultimate function of the heart is to "pump" the blood for delivery to the cells of the body by generating a sufficient pressure gradient, such a function can only be conducted through the deformation, the collective dilatation and distortion, of the cardiac muscle. Hence, normal motion of the cardiac muscle is crucial for its normal function, and any alteration in its motion could prove harmful for the heart. Various pathologies of the heart often arise from such abnormal motions.

1.5 Assumptions Made for the Heart with Mathematical Implications

While the mechanical behavior of heart is undoubtedly ananalytical, certain assumptions can be made that allow it to be relatively analytical with an acceptable degree of uncertainty given the interest of this work in modeling passive behavior, the stepping stone for modeling active myocardial behavior. In general, the exhibited behavior of the heart is non-linear, heterogeneous, inelastic, and anisotropic. However, for the purposes of this work, the elasticity of the heart will be assumed to be in the hyperelastic limit, which implies that the mechanical work done is stored as strain energy. The strain energy can then be used to deduce the constitutive model. Additionally, the focus of this work does not encompass quantifying residual stresses, so the heterogeneity assumption will not be as relevant. Instead, homogeneity can be assumed, which would allow for the use of a small section of myocardium to derive a model, and then allowing that model to be generalized for the whole heart, assuming the level of uncertainty is acceptable. Finally, because there are three orthogonal directions along which the mechanical behavior primarily varies, the myocardium can be assumed to be orthotropic. Therefore, such

assumptions deem modeling the mechanical behavior of the heart possible to be expressed in an analytical form.

1.6 Choice of Coordinate System

In order to quantify the behavior of the heart, the analysis must be conducted in an appropriate coordinate system. Experiments, namely mechanical testing of soft tissues, are usually done within lab coordinates (made up of bases in the longitudinal, circumferential, and radial directions) which are Cartesian in nature ($\mathbf{e}_1$, $\mathbf{e}_2$, $\mathbf{e}_3$). However, for such measurements to be physically relevant for the heart, material coordinates, or namely cardiac coordinates, shall be implemented. Furthermore, the basis vectors for this coordinate system ($\mathbf{e}_f$, $\mathbf{e}_s$, $\mathbf{e}_n$) are determined relative to the fibers of the heart, as demonstrated in **Figure 3** (Li et al. 2020). The basis vectors are made from three orthogonal directions: the fiber direction, which is parallel to the orientation of the fibers of the heart; the cross-fiber (i.e., sheet) direction, which is in the same plane as fiber as well as orthogonal to it; and the normal direction, which is orthogonal to both. Because myocardial deformation is the focus of this work, cardiac coordinates shall be implemented as the coordinate system of choice.

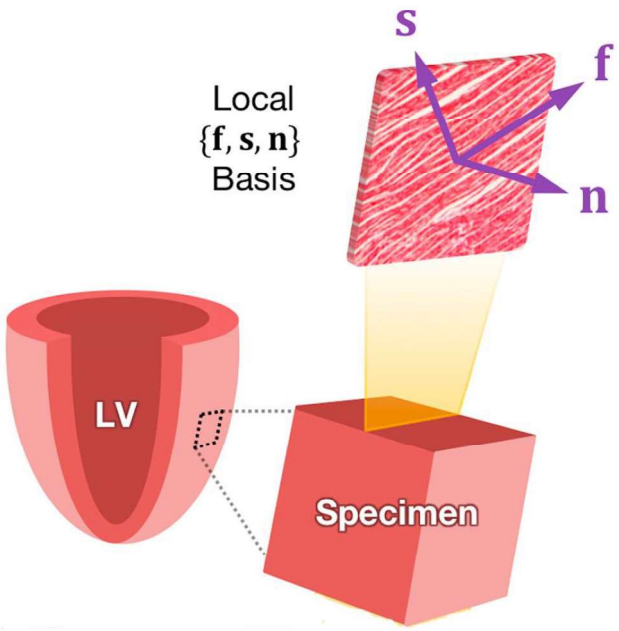

Figure 3. Cardiac coordinates basis directions for the myocardium. Reprinted from (Li et al, 2020)

1.7 Polar Decomposition Theorem

As the heart enters and progresses through the cardiac cycle, its fibers shorten and elongate as it contracts and relaxes, respectively. Additionally, the fibers deform via undergoing shear and rotation or collectively twist. Given that various diseases interfere with the normal harmony of the aforementioned modes of motion, decoupling these motions mathematically is of utmost importance as it allows the assessment of each mode of motion in isolation from the other modes, the stretches from the rotations in particular. Traditionally, that is achieved by the polar decomposition theorem, demonstrated by **Equation 1**.

$$\mathbf{F} = \mathbf{RU} = \mathbf{VR} \qquad \textbf{(Eq. 1)}$$

where **F** is the *deformation gradient tensor*, **R** is the *rotation tensor*, **U** is the *right stretch tensor*, and **V** is the *left stretch tensor*.

1.8 QR Decomposition Theorem

While the polar decomposition theorem proves to be a valuable tool to decouple the deformation gradient tensor into rotation and stretch, it is computationally inconvenient due to (1) its requirement of an eigenvalue decomposition for the right Cauchy-Green tensor $\boldsymbol{C}$ followed by a matrix inversion to find the rotation tensor $\boldsymbol{R}$; (2) the invariants do not possess a direct physical meaning for the modes of cardiac deformation experimentally (Srinivasa 2012).

Therefore, Srinivasa proposed an improved theorem that utilizes an upper triangular matrix to decouple deformation into stretch and pure rotation, known as the QR decomposition, expressed in **Equation 2** (Srinivasa 2012). This theorem improves on its predecessor in **Equation 1** by (1) eigenvalues or eigenvectors are not required to express rotation; (2) the upper triangular matrix $\boldsymbol{R}$ is related to the right Cauchy-Green tensor $\boldsymbol{C}$ through a Cholesky factorization; (3) the six components of the upper triangular matrix $\boldsymbol{R}$, the shear and orthogonal stretches, have direct physical meaning that is experimentally measurable; (4) it provides a relatively more inclusive and unified method to study the deformation of the major crystal classes, including soft tissues. (Srinivasa 2012).

$$\mathbf{F} = \mathbf{QR} \qquad \textbf{(Eq. 2)}$$

where **F** is the *deformation gradient tensor*, **Q** is the *pure rotation tensor*, and **R** is the *right upper triangular matrix*, consisting of the orthogonal and shear stretches.

The motion of the heart occurs as a result of the forces generated within it. To obtain the deformation gradient which describes the motion, finding the stresses and relating them to the strains are also crucial to understanding and analyzing the behavior of the heart. Such equations relating the stresses to the strains are known as constitutive relations, and for the heart, the constitutive relation (**Equation 3**) is as follows (Costa et al. 1999):

$$\boldsymbol{\sigma} = \frac{2}{J}\mathbf{F}\frac{\partial W}{\partial \mathbf{C}}\mathbf{F}^{\mathbf{T}} - p\mathbf{I} \qquad \textbf{(Eq. 3)}$$

where **σ** is the *Cauchy stress tensor, J* is the *Jacobian* which is the determinant of **F** in this case [J = **det(F)**], **F** is the *deformation gradient tensor*, *W* is the *strain energy function*, **C** is the *right Cauchy-Green deformation tensor*, $\mathbf{F}^{\mathbf{T}}$ is the *transpose of the deformation gradient tensor*, *p* is the *pressure* which is one-third of the trace of the Cauchy stress [p = $\frac{1}{3}$ **tr(σ)**], and ***I*** is the identity tensor.

1.9 Cardiac Modes of Deformation Resulting from QR Decomposition

As a consequence of QR decomposition, Criscione et al. defined six strain parameters (α_i) which quantify the modes of deformation for the heart as an alternative to the Green strains required in the Fung model (Criscione et al. 2002). Each strain parameter characterizes the deformation of the heart in a specific mode of motion. These parameters are:

$$\alpha_1 = \mathbf{ln}\, J \qquad \textbf{(Eq. 4a)}$$

$$\alpha_2 = \frac{3}{2}\ln \lambda_f \quad \textbf{(Eq. 4b)}$$

$$\alpha_3 = 2\ln \zeta \quad \textbf{(Eq. 4c)}$$

$$\alpha_4 = \phi_{fs} \quad \textbf{(Eq. 4d)}$$

$$\alpha_5 = \phi_{fn} \quad \textbf{(Eq. 4e)}$$

$$\alpha_6 = \phi_{sn} \quad \textbf{(Eq. 4f)}$$

where $\boldsymbol{\alpha_1}$, $\boldsymbol{\alpha_2}$, and $\boldsymbol{\alpha_3}$ represent normal strains, namely the volume strain, distortional "fiber" strain, and the laminar thickening strain, respectively (Criscione et al. 2002). In addition, $\boldsymbol{\alpha_4}$, $\boldsymbol{\alpha_5}$, and $\boldsymbol{\alpha_6}$ represent shear strains, which are the motions of the material planes along their orthogonal axes (Criscione et al. 2002). Furthermore, $\boldsymbol{\alpha_4}$ represents the motion of the fiber plane along the sheet axis; $\boldsymbol{\alpha_5}$ represents motion of the fiber plane along the normal axis; and $\boldsymbol{\alpha_6}$ represents motion of the sheet plane along the normal axis (**Figure 4**).

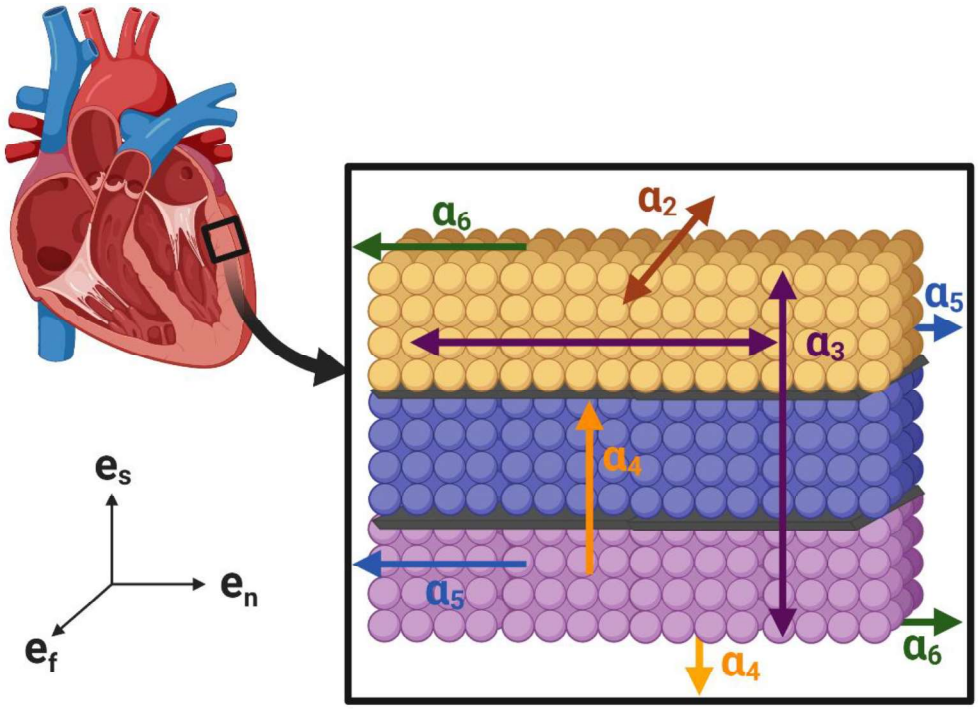

Figure 4. The modes of motion of the heart quantified by the strain attributes that result from QR decompositions. α_1 is not shown because it is equal to zero for incompressibility.

Such modes are relatively more representative of the physical deformation of the heart, and they decrease the degeneracy of the strain energy function (W) as fewer variables are required to generate the best fit. In other words, finding a $W(E_{ff}, E_{ss}, E_{nn})$ that fits biaxial data will require solving a system of two equations with three unknowns, which implies an infinity of solutions. However, finding a $W(\alpha_2, \alpha_3)$ that fits biaxial data will require solving a system of two equations with two unknowns, which results in a unique solution compared with the former W.

1.10 The Strain Energy Function

As a consequence of the hyperelastic limit, the strain energy function is a function that relates the Green strains to potential energy. It describes the energy stored or released within the soft tissue upon deformation due to changes in the strains. Y.C. Fung, the father of modern biomechanics, developed an equation that describes the strain energy function for a soft tissue (**Equation 5**) (Fung 1967, 1973, 1983, 1990, 1993, 1995):

$$W = \frac{1}{2}c(e^{Q} - 1) \qquad \textbf{(Eq. 5)}$$

where W is the *strain energy function*, c is a *material constant*, and Q is the *material stiffness function*, which is a function of the Green strains that varies based on the deformation profile of the soft tissue. For an incompressible, orthotropic heart, the function Q is:

$$Q = b_{ff}{E_{ff}}^2 + b_{ss}{E_{ss}}^2 + b_{nn}{E_{nn}}^2 + 2b_{fs}{E_{fs}}^2 + 2b_{sn}{E_{sn}}^2 + 2b_{fn}{E_{fn}}^2 \qquad \textbf{(Eq. 6)}$$

where $\boldsymbol{E_{ff}}$, $\boldsymbol{E_{ss}}$, $\boldsymbol{E_{nn}}$, $\boldsymbol{E_{fs}}$, $\boldsymbol{E_{sn}}$, and $\boldsymbol{E_{fn}}$ are components of the Green Strain tensor in cardiac coordinates, and $\boldsymbol{b_{ff}}$, $\boldsymbol{b_{ss}}$, $\boldsymbol{b_{nn}}$, $\boldsymbol{b_{fs}}$, $\boldsymbol{b_{sn}}$, and $\boldsymbol{b_{fn}}$ are material stiffness constants whose respective values depend on the deformation profile of the soft tissue within the experiment. Due to the symmetry of the Green Strain Tensor, $\boldsymbol{E_{fs}} = \boldsymbol{E_{sf}}$, $\boldsymbol{E_{sn}} = \boldsymbol{E_{ns}}$, and $\boldsymbol{E_{fn}} = \boldsymbol{E_{nf}}$. As shown in **Equation 6**, six strains are required to obtain the strain energy function, which indicate high degeneracy for the strain energy function.

1.11 A Gap in the Field

While the current model for myocardial stress with the assumptions of incompressibility and orthotropy, provided in **Equation 3**, is a powerful technique to calculate the different stresses, it is not devoid of limitations. First, because the relationship between the stresses and strains in the heart is indirect, finding the stresses is computationally exhausting. Second, the strain energy function in **Equation 3** is a function of high degeneracy due its dependency on six strains, which inherently makes stress transitively a function of high degeneracy as well; furthermore, in biaxial testing, there are three unknowns ($\frac{\partial W}{\partial E_{ff}}$, $\frac{\partial W}{\partial E_{ss}}$, $\frac{\partial W}{\partial E_{nn}}$) yet two equations, resulting in an infinite number of solutions. Third, given the deformation gradient is conventionally decoupled by the polar decomposition theorem, the resulting stretches do not have a direct physical meaning.

In an attempt to address these limitations, Criscione et al. proposed a modified constitutive theory that defines the stress in terms of more physically and experimentally tractable "strain parameters" (Criscione et al. 2002). This model for incompressible and orthotropic behavior is expressed below in **Equation 7** (Criscione et al. 2002):

$$\boldsymbol{\sigma} = \frac{1}{J}\sum_{\mathrm{i}=2}^{6}\frac{\partial W}{\partial \alpha_i}\mathbf{A_i} - p\mathbf{I} \qquad \textbf{(Eq. 7)}$$

where $\boldsymbol{\sigma}$ is the *Cauchy stress tensor, J* is the *Jacobian* which is the determinant of **F** in this case [J = **det(F)**], W is the *strain energy function*, α_i is the *strain parameter*, $\mathbf{A_i}$ is the *deviatoric tensor*, p is the *pressure* which is one-third of the trace of the Cauchy stress [$p = \frac{1}{3}$ **tr(σ)**], and $\boldsymbol{I}$ is the identity tensor.

Furthermore, Criscione et al. found a general solution for *W* that satisfies **Equation 7** above and takes into consideration the parameters possible for incompressible, orthotropic behavior in the following equation (Criscione et al. 2002).

$$W = \begin{pmatrix} W_0 + q_2\alpha_2 + q_3\alpha_3 + \frac{1}{2}g_{22}\alpha_2^2 + \frac{1}{2}g_{33}\alpha_3^2 + g_{23}\alpha_2\alpha_3 + \frac{1}{2}g_{44}\alpha_4^2 \\ + \frac{1}{2}g_{55}\alpha_5^2 + \frac{1}{2}g_{66}\alpha_6^2 + g(\alpha_2, \alpha_3) + H(\alpha_2, \alpha_3, \alpha_4, \alpha_5, \alpha_6) \end{pmatrix} \quad \textbf{(Eq. 8)}$$

where q_2 and q_3 are the *residual stresses*, g_{22}, g_{33}, g_{44}, g_{55}, and g_{66} are the scalar moduli, and $g(\alpha_2, \alpha_3)$ and *H* are functions which denote higher order behavior.

However, while *W* in **Equation 8** does indeed take into consideration all the possible orders of behavior, it does not display an explicit form for higher order behavior, a characteristic of soft tissues behavior. Also, to go beyond data fitting, particularly one-to-one mapping between the material coefficients and material function (linking it to the multiscale structure of the myocardium), the degeneracy would have to be minimized as it would require uniqueness for the material parameters, so that the resulting solution is closer to the true model of the heart. Therefore, this is a gap that must be addressed.

1.12 Significance

Because the strain energy function acts as a mathematical "bridge" that relates the myocardial strains to their respective stresses (**Equation 3**), the work in this thesis is fundamental in developing constitutive models describing myocardial deformation with low degeneracy. The relationship between the strain and the stress for the heart mediates the physiological functions of the heart, and changes in such a relationship may also

explain some pathophysiological phenomena that lead to motion abnormalities within the myocardium. Such a relationship lies at the heart of understanding the underlying mechanics and behavior of the myocardium.

In addition, this work is critical in creating a model that can be used by the community of mathematicians, engineers, and physicists working in the area of cardiac biomechanics to be able to create simulations that accurately capture the function of the myocardium as well as establish lab experiments that are closer to accurate in mimicking myocardial deformation, such as cell culture, organ on a chip, and tissue engineering applications. Finally, these models are important in designing cardiac devices that are sounder solutions to various types of cardiovascular disease, the leading cause of death worldwide.

1.13 Goal of This Work

This work seeks to decrease the degeneracy of the Fung Strain Energy Function by proposing a modified function obtained by the QR decomposition that would yield the stresses using less strain parameters (five rather than six). Furthermore, such strain parameters are more experimentally relevant and physically meaningful for the heart. This work will utilize biaxial testing data conducted by Humphrey et al. to infer how myocardial strain energy is perturbed relative to each strain parameter and use that to derive a functional form (Humphrey et al. 1990). Subsequently, the functional form will then be used to predict the stresses from the given strains, and the predicted stresses will then be compared with the measured stresses for evaluation of the accuracy of the model.

CHAPTER II

METHODS

2.1 Introduction

To compare data, published biaxial testing data of a myocardium specimen was used from Humphrey et al., and a constitutive model was developed to fit the data (Humphrey et al. 1990). The model was then compared with the widely used constitutive relation derived from the Fung strain energy function. Finally, the uncertainty in each model was calculated to determine the degree of certainty for the fit. To formulate the constitutive relation of interest, five basic steps were adopted in this work (Humphrey 2002):

i. delineation of the general characteristics of interest
ii. establishing an appropriate theoretical framework for quantification
iii. identification of specific functional forms of the constitutive relations
iv. calculation of the values of the associated material parameters
v. evaluation of the predictive capability of the final relation.

2.2 Biaxial Testing Data

Data were retrieved from biaxial testing of a thin slab of myocardium, where stretches were conducted along the principal directions of the stresses (Humphrey et al. 1990) (**Figure 5**). Furthermore, because the myocardium is thin, stresses in the $\mathbf{e}_3$ direction are negligible. The specimen tethers were aligned with the fiber and cross-fiber direction,

which makes a coordinate transformation from laboratory coordinates (i.e., cartesian coordinates with $\mathbf{e}_1$, $\mathbf{e}_2$, and $\mathbf{e}_3$ as the bases) to material coordinates (i.e., cardiac coordinates with $\mathbf{e}_f$, $\mathbf{e}_s$, and $\mathbf{e}_n$ as the bases) unnecessary as the fiber orientation angle (angle of fibers relative to Cartesian coordinates) can be thought of as zero degrees.

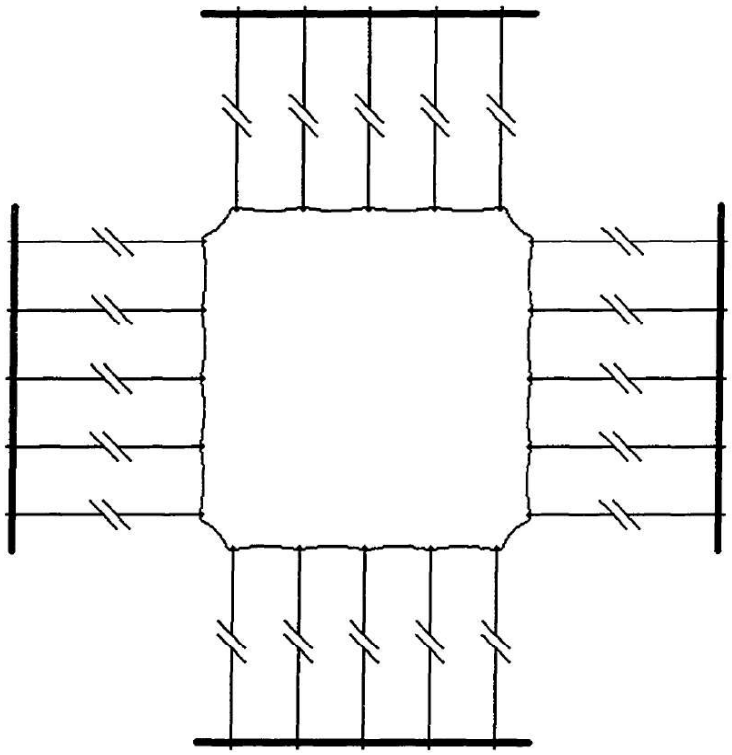

Figure 5. Biaxial stretching apparatus in the reference configuration. Reprinted from (Criscione 1999)

For biaxial testing, stretching was conducted in two directions, the fiber and cross-fiber directions. This led the apparatus to produce the loads, and as a result, the resulting Cauchy stresses were computed by Humphrey (Humphrey et al. 1990). **Figures 6 – 11** demonstrate both the fiber and cross-fiber (sheet) stretches, their respective Cauchy

stresses, and their stretch-stress relationship. There were two stretching protocols that were used to produce two sets of biaxial data. The first set was a result of setting the fiber stretch constant ($\lambda_f = 1.2$) and varying the cross-fiber stretch (λ_s) (**Figures 6 – 8**). This data set was used to find a functional form for the strain energy function (W). The second data set, where both the fiber and cross-fiber stretch were varied, was used to then solve for the material stiffness constants of the model that best fits the data (**Figures 9 – 11**).

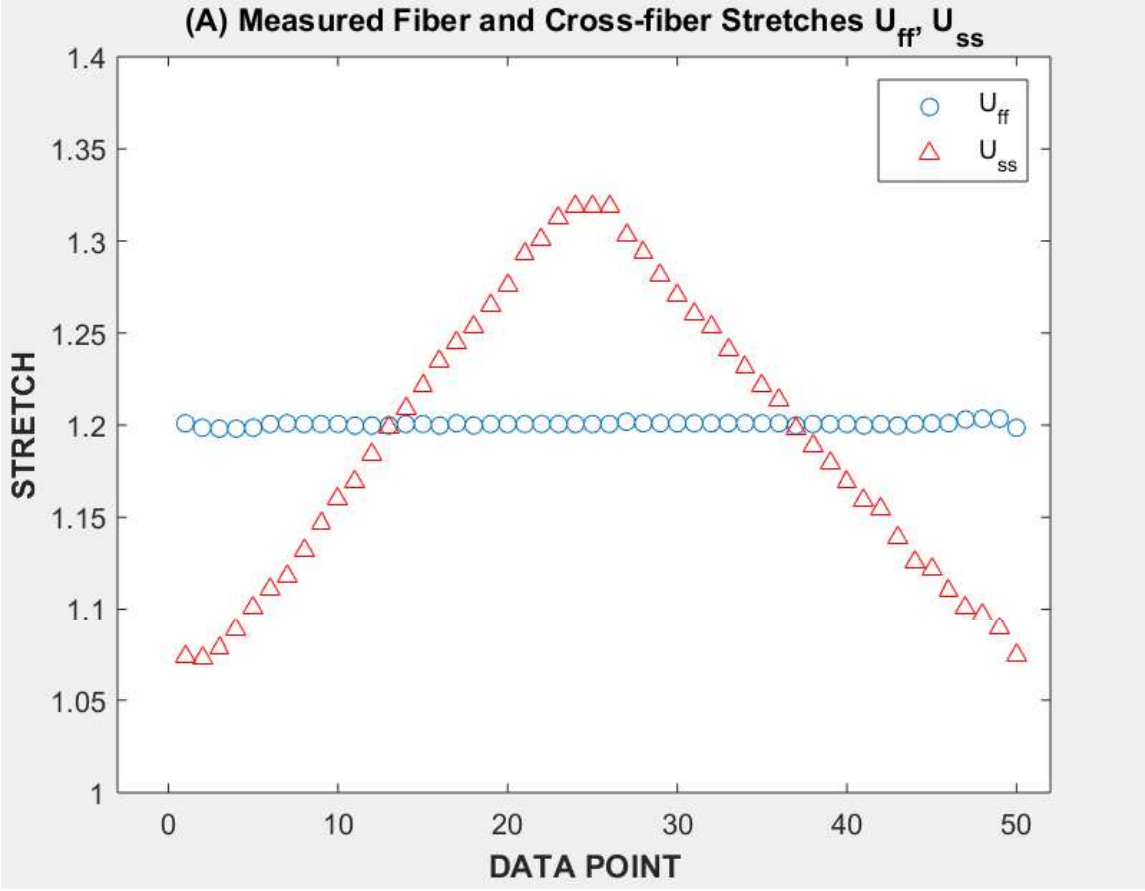

Figure 6. The first set of fiber and cross-fiber stretches applied to the myocardium specimen; the blue circles represent fiber stretch, and the red triangles represent the cross-fiber (sheet) stretches. Reprinted from (Humphrey et al. 1990).

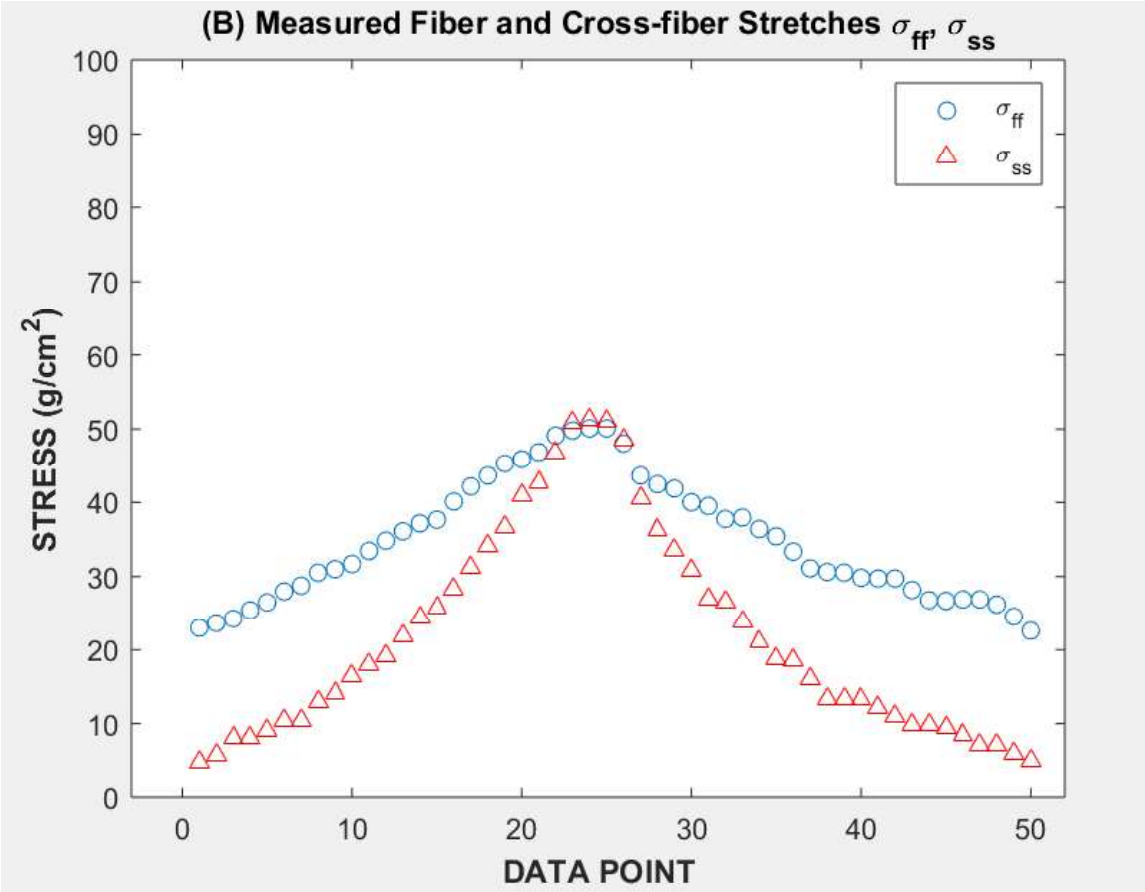

Figure 7. Fiber stresses (circles) and sheet stresses (triangles). Reprinted from (Humphrey et al. 1990)

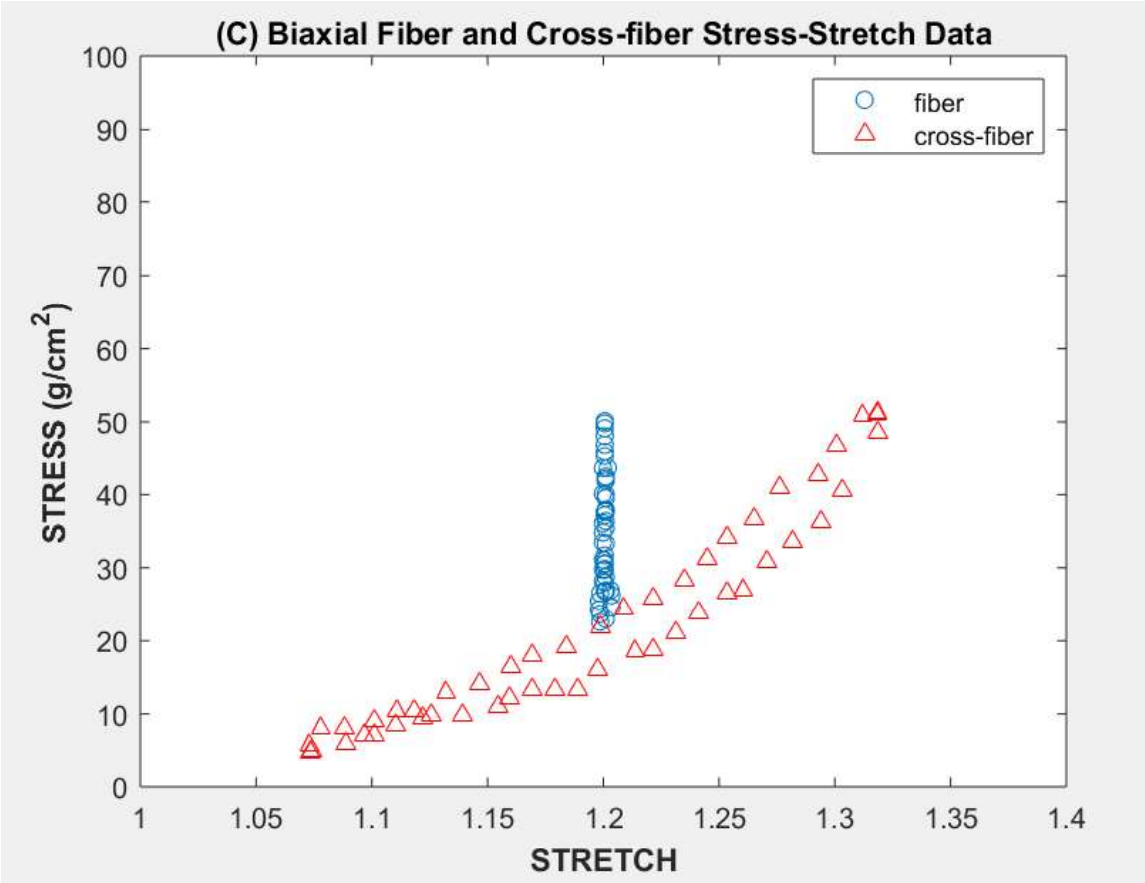

Figure 8. The fiber and sheet stress-stretch relationships. Reprinted from (Humphrey et al. 1990)

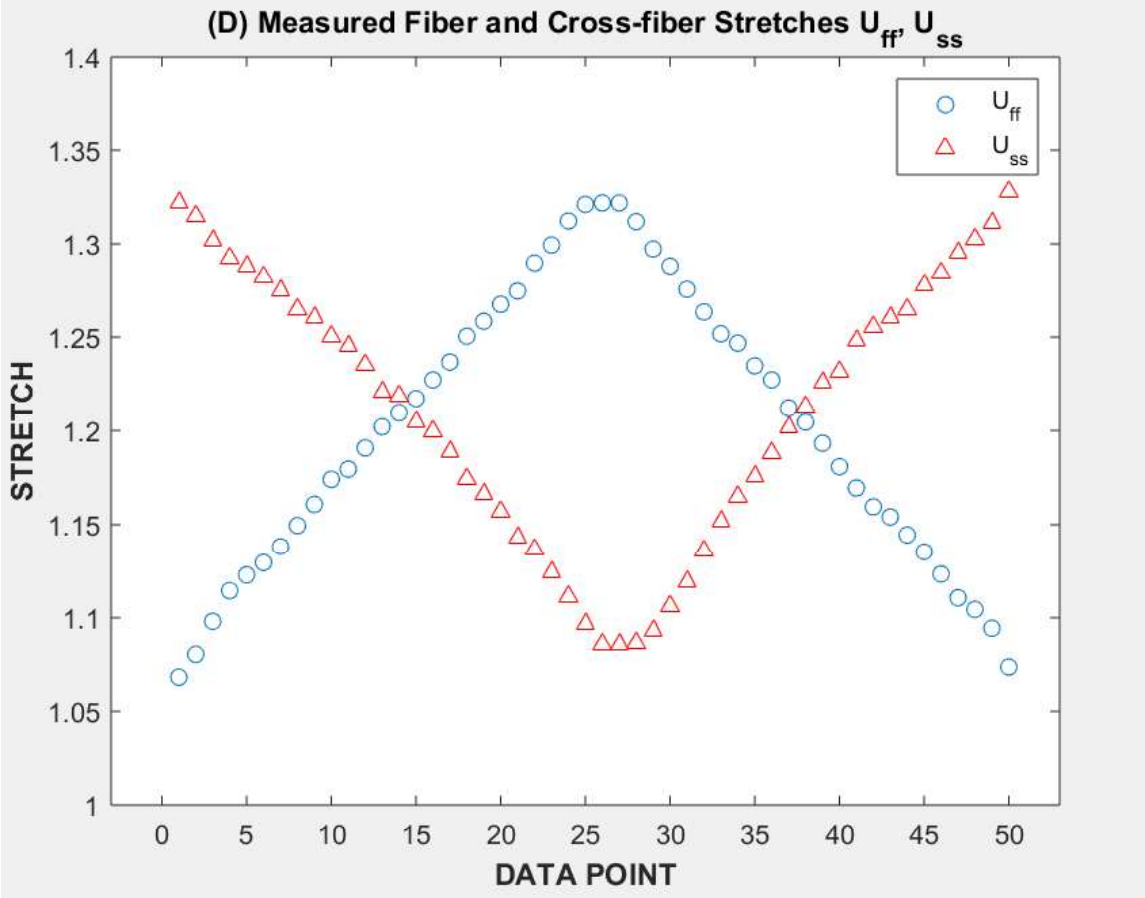

Figure 9. The second set of fiber and sheet stretches applied to the myocardium specimen. Reprinted from (Humphrey et al. 1990)

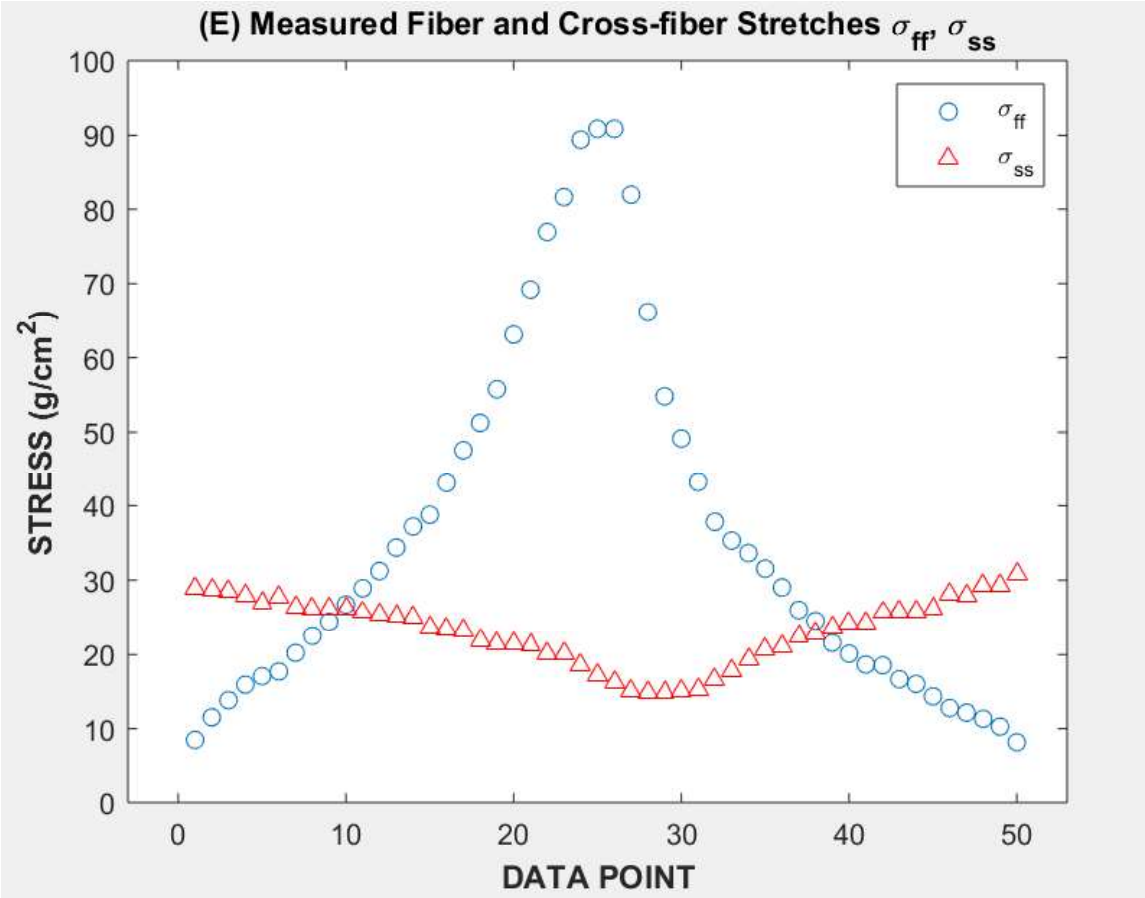

Figure 10. The second set of fiber and sheet stresses. Reprinted from (Humphrey et al. 1990)

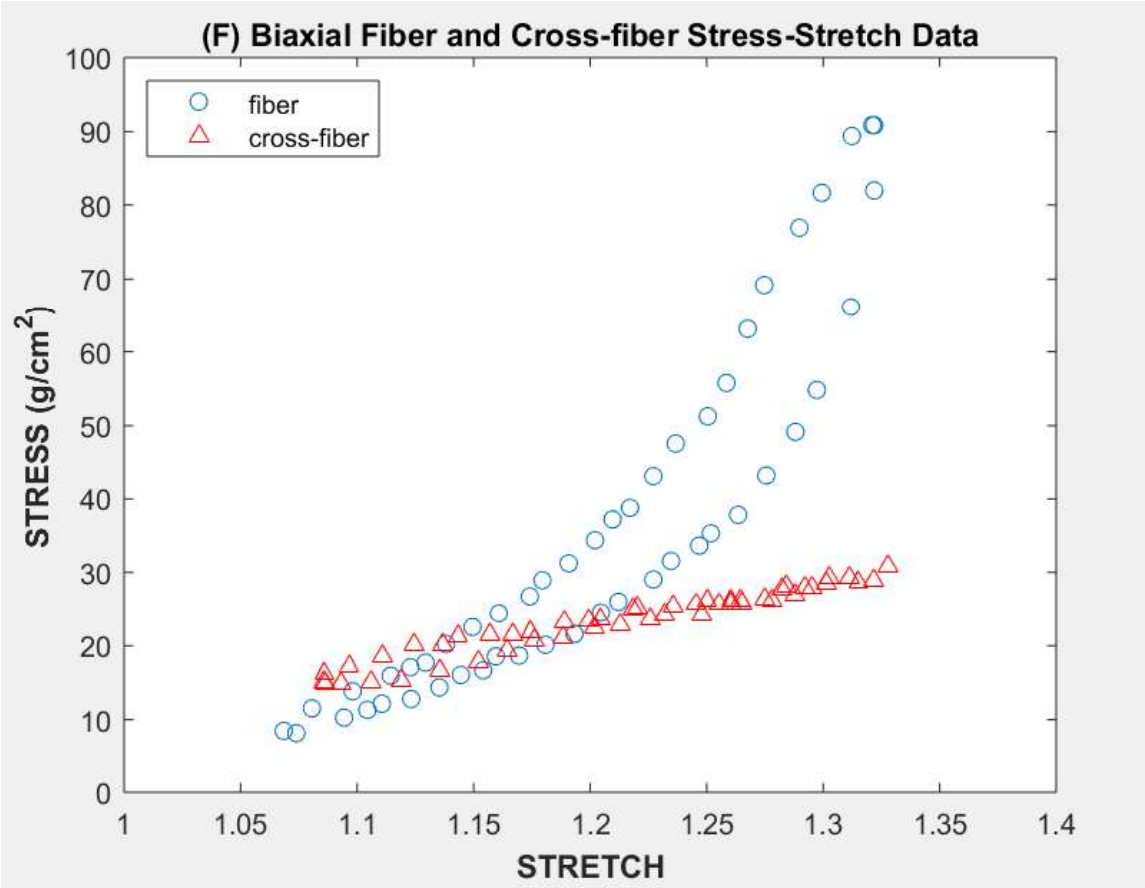

Figure 11. The second set of fiber and sheet stress-stretch relationships. Reprinted from (Humphrey et al. 1990)

2.3 General Characteristics & Assumptions for the Myocardium

In the introduction, it was established that the myocardium at the tissue level exhibits behavior that is characterized as being nonlinear, anisotropic, heterogeneous, and inelastic. However, for the purpose of this work, some of these assumptions were revised while maintaining an acceptable degree of uncertainty. First, the myocardium was assumed to be orthotropic, as there were three mutually orthogonal directions along which the mechanical properties vary (i.e., the fiber, cross-fiber, and normal directions), demonstrated in **Figure 3**. Additionally, while the myocardium is indeed anisotropic, a

constitutive relation will be derived and verified using data obtained from mechanical testing of a thin slab of myocardium extracted from within the wall of the heart (Humphrey et al. 1990). Hence, homogeneity can be assumed, allowing the constitutive relation to be generalized for the entire heart. Additionally, because the cardiomyocytes are mainly filled with water, which has a high bulk modulus, the myocardium can be assumed to be incompressible. Finally, rather than assuming the myocardium to be inelastic, the myocardial specimen has both solid-like and fluid-like properties, allowing the myocardium to be approximated as a viscoelastic material. However, given the mechanics of viscoelasticity is not currently well-established, the elasticity of the myocardium will be assumed to be hyperelastic, which is justified by the fact that the work done on the myocardium is stored as strain energy.

2.4 Establishing an Appropriate Theoretical Framework

A drawn inspiration to extend the work of Criscione et al. and Srinivasa, the upper triangular matrix decomposition (i.e., QR decomposition) is utilized as the overarching framework for this work to derive a new strain energy function for the incompressible, orthotropic myocardium (Criscione et al. 2002; Srinivasa 2012). Considering a typical section of the myocardium used for the experiments (**Figure 5**), the coordinate system utilized is the cardiac coordinate system with bases of $\mathbf{e}_f$, $\mathbf{e}_s$, $\mathbf{e}_n$ for the fiber, cross-fiber, and normal direction, respectively. To quantify its deformation within an appropriate reference frame, there are two configurations referred in this work; the reference configuration, which is undeformed, and the current configuration, which is deformed.

The reference configuration represents the undeformed slab of myocardium (**Figure 5**), and the current configuration is the myocardium when it is stretched along either axis or both axes, represented by the fiber and the cross-fiber directions.

2.5 The Kinematics of Biaxial Testing

To map the current configuration of the myocardium specimen to its reference configuration, the following transformation equations were used (Humphrey, 1990):

$$x_1 = \lambda_1 X_1 + \kappa_1 X_2 \quad \textbf{(Eq. 9a)}$$

$$x_2 = \lambda_2 X_2 + \kappa_2 X_1 \quad \textbf{(Eq. 9b)}$$

$$x_3 = \lambda_3 X_3 \quad \textbf{(Eq. 9c)}$$

where $\boldsymbol{X_i}$ and $\boldsymbol{x_i}$ represent the coordinates of a point on the material in the reference and current configuration, respectively, and λ_i and κ_i are the stretch and the in-plane shear components of the deformation gradient tensor **F**, respectively (Humphrey et al. 1990). The bases of these coordinates are Cartesian. Due to the assumption of homogeneity, it can be assumed that this mapping can be generalized to include every material point on the specimen (Humphrey et al. 1990).

To find the components of **F**, the material gradient of the position vector of the current configuration (i.e., $\mathbf{F} = \frac{\partial \mathbf{x}}{\partial \mathbf{X}}$) was found. Furthermore, because there were no in-plane shears, the shear components were zero (i.e., $\kappa_i = 0$) (Humphrey, 1990). The radial stretch (λ_3) can be found from the volume strain, **det(F)**, which is equal to 1 due to the

incompressibility constraint. This results in $\lambda_3 = (\lambda_1\lambda_2)^{-1}$. Hence, the final form of **F** is represented by:

$$\mathbf{F} = \lambda_1\mathbf{e_1} \otimes \mathbf{e_1} + \lambda_2\mathbf{e_2} \otimes \mathbf{e_2} + \lambda_3\mathbf{e_3} \otimes \mathbf{e_3} \quad \textbf{(Eq. 10)}$$

To find the right Cauchy-Green deformation tensor **C**, the transpose of **F** needs to first be found and then be operated on **F** (i.e., $\mathbf{C} = \mathbf{F}^T\mathbf{F}$). Therefore, in direct notation, **C** becomes:

$$\mathbf{C} = {\lambda_1}^2\mathbf{e_1} \otimes \mathbf{e_1} + {\lambda_2}^2\mathbf{e_2} \otimes \mathbf{e_2} + {\lambda_3}^2\mathbf{e_3} \otimes \mathbf{e_3} \quad \textbf{(Eq. 11)}$$

Because the strain energy function in **Equation 5** is expressed as an implicit function of the Green strains, it would prove useful to find the Green strain tensor **E**, given that it will also be used to calculate the Cauchy stress using **Equation 3**. Because $\mathbf{E} = \frac{1}{2}(\mathbf{C} - \mathbf{I})$, the expression for **E** becomes:

$$\mathbf{E} = \frac{1}{2}\left[({\lambda_1}^2 - 1)\mathbf{e_1} \otimes \mathbf{e_1} + ({\lambda_2}^2 - 1)\mathbf{e_2} \otimes \mathbf{e_2} + ({\lambda_3}^2 - 1)\mathbf{e_3} \otimes \mathbf{e_3}\right] \quad \textbf{(Eq. 12)}$$

To allow the computation of the stresses and the strains to be more relevant for the heart, a coordinate transformation must be applied. Furthermore, the previous equations (**Equations 9 – 12**) are in lab coordinates, which are Cartesian in nature. However, for such measurements to be physically relevant for the heart, cardiac coordinates (i.e., material coordinates) must be used. Additionally, a coordinate transformation will enable the use of the strain parameters that were derived from QR decomposition as they can only be computed from stretches in cardiac coordinates. Therefore, for thin slabs of myocardium excised in parallel to the epicardial or endocardial surfaces, the unit vector transformation from Cartesian into cardiac coordinates is:

$$\mathbf{N} = \cos \Phi(X_3)\mathbf{e_1} + \sin \Phi(X_3)\,\mathbf{e_2} \qquad \textbf{(Eq. 13)}$$

where $\Phi(X_3)$ is the fiber orientation angle measured with respect to $\mathbf{e_1}$ (Humphrey and Yin 1989). However, because the stretches were conducted parallel with the fiber direction and perpendicular to it, i.e., in the fiber and cross-fiber directions, $\Phi = 0^o$. As a result, the stretches and the strains are comparable in both coordinate systems.

To calculate the strain parameters that result from QR decomposition, the upper triangular stretches must first be found. Due to the convention of **R** representing a rotation tensor in continuum mechanics, **f** will be used instead to denote the upper triangular matrix of stretches. Because $\mathbf{C} = \mathbf{f}^T\mathbf{f}$, $\mathbf{E} = \frac{1}{2}(\mathbf{f}^T\mathbf{f} - \mathbf{I})$ (Srinivasa 2012). Hence, **f** can be calculated from **E** by the following equations:

$$f_{ff} = \sqrt{2E_{ff} + 1} \qquad \textbf{(Eq. 14a)}$$

$$f_{fs} = \frac{2E_{fs}}{f_{ff}} \qquad \textbf{(Eq. 14b)}$$

$$f_{fn} = \frac{2E_{fn}}{f_{ff}} \qquad \textbf{(Eq. 14c)}$$

$$f_{ss} = \sqrt{2E_{ss} - {f_{fs}}^2 + 1} \qquad \textbf{(Eq. 14d)}$$

$$f_{sn} = \frac{1}{f_{ss}}(2E_{sn} - f_{fs}f_{fn}) \qquad \textbf{(Eq. 14e)}$$

$$f_{nn} = \sqrt{2E_{nn} - \left({f_{fn}}^2 + {f_{sn}}^2\right) + 1} \qquad \textbf{(Eq. 14f)}$$

Next, the kinematic variables from Criscione et al. were used to calculate the strain parameters (Criscione et al. 2002). These kinematic variables are:

$$J = f_{ff} f_{ss} f_{nn} \quad \textbf{(Eq. 15a)}$$

$$\lambda_f = J^{-1/3} f_{ff} \quad \textbf{(Eq. 15b)}$$

$$\zeta = J^{-1/3} {\lambda_f}^{1/2} f_{nn} \quad \textbf{(Eq. 15c)}$$

$$\phi_{fs} = J^{-1/3} {\lambda_f}^{-1} f_{fs} \quad \textbf{(Eq. 15d)}$$

$$\phi_{fn} = J^{-1/3} {\lambda_f}^{-1} f_{fn} \quad \textbf{(Eq. 15e)}$$

$$\phi_{sn} = J^{-1/3} {\lambda_f}^{1/2} \zeta f_{sn} \quad \textbf{(Eq. 15f)}$$

Hence, using **Equations 4a-f**, the strain attributes can now be calculated. Because the experimental data is from biaxial testing in the fiber and cross-fiber directions, $\alpha_4 = \alpha_5 = \alpha_6 = 0$. In addition, due to the incompressibility constraint, α_1 is also 0 as J is defined to be equal to 1 (i.e., **det(F)** = 1).

2.6 The Functional Form of the Strain Energy Function (W)

To find the functional form of the strain energy function $W(\alpha_2, \alpha_3)$, the functional form of the perturbation of W with respect to each strain parameter relevant to biaxial testing (i.e., the partial derivatives of W) was estimated from the first set of data in **Figures 6 – 8**. Furthermore, the data set in **Figures 6** shows little to no change in α_2, yet there is change in α_3. To find the partial derivatives, the measured stresses from the first data set (**Equation 16**) were used utilizing the following equations from Criscione et al:

$$\boldsymbol{\sigma} = \sigma_{ff} \mathbf{e_f} \otimes \mathbf{e_f} + \sigma_{ss} \mathbf{e_s} \otimes \mathbf{e_s} \quad \textbf{(Eq. 16)}$$

$$\frac{\partial W}{\partial \alpha_2} = J(\mathbf{L_f} : \boldsymbol{\sigma}) \quad \textbf{(Eq. 17)}$$

$$\frac{\partial W}{\partial \alpha_3} = J(\mathbf{L_\zeta} : \boldsymbol{\sigma}) \quad \textbf{(Eq. 18)}$$

where $\mathbf{L_f}$ and $\mathbf{L_\zeta}$ are deviatoric kinematic tensors (i.e., their trace is zero), which are mathematically expressed as (Criscione et al. 2002)

$$\mathbf{L_f} = \frac{2}{3}\mathbf{e_f} \otimes \mathbf{e_f} - \frac{1}{3}(\mathbf{e_s} \otimes \mathbf{e_s} + \mathbf{e_n} \otimes \mathbf{e_n}) \quad \textbf{(Eq. 19)}$$

$$\mathbf{L_\zeta} = \frac{1}{2}(\mathbf{e_n} \otimes \mathbf{e_n} - \mathbf{e_s} \otimes \mathbf{e_s}) \quad \textbf{(Eq. 20)}$$

Hence, using the solution of Criscione et al. for W in **Equation 8** to find its partial derivatives in **Equation 17** and **18**, and contracting **Equation 19** and **20** with **Equation 16**, **Equation 17** and **18** can be re-expressed, respectively, as follows:

$$\frac{\partial W}{\partial \alpha_2} = \frac{\partial g(\alpha_2, \alpha_3)}{\partial \alpha_2} + g_{22}\alpha_2 + g_{23}\alpha_3 = \frac{2}{3}\sigma_{ff} - \frac{1}{3}\sigma_{ss} \quad \textbf{(Eq. 21)}$$

$$\frac{\partial W}{\partial \alpha_3} = \frac{\partial g(\alpha_2, \alpha_3)}{\partial \alpha_3} + g_{23}\alpha_2 + g_{33}\alpha_3 = -\frac{1}{2}\sigma_{ss} \quad \textbf{(Eq. 22)}$$

Therefore, **Equations 21** and **22** were used to derive the functional form of $W(\alpha_2, \alpha_3)$ from the first set of biaxial data by finding a function that best fits the data using the curve fitting tool in MATLAB.

2.7 Calculation of the Material Parameters

Upon finding the functional form of $W(\alpha_2, \alpha_3)$ from the first data set, the second data set (**Figures 9 – 11**) was used to solve for the unknown material constants (i.e., material parameters) that uniquely characterized the myocardium specimen used in the experiment, and by homogeneity, the entire myocardium to a certain acceptable degree of

uncertainty. A code was written in MATLAB using the previous equations to find the numerical solution for the material constants that best fit the functional form of $W(\alpha_2, \alpha_3)$ using a Marquardt-Levenberg nonlinear regression that minimizes the sum of the squares of errors between the experimentally measured and theoretically predicted partial derivatives of the strain energy function $W(\alpha_2, \alpha_3)$, shown in **Equation 23**.

$$MSE_{QRW} = \left[\left(\frac{\partial W}{\partial \alpha_2}\right)^{pred.} - \left(\frac{\partial W}{\partial \alpha_2}\right)^{meas.}\right]^2 + \left[\left(\frac{\partial W}{\partial \alpha_3}\right)^{pred.} - \left(\frac{\partial W}{\partial \alpha_3}\right)^{meas.}\right]^2 \quad \textbf{(Eq. 23)}$$

where MSE_{QRW} is the minimized squares of errors of the strain energy function W derived from the QR model (Appendix A).

2.8 Evaluation of the Predictive Capability of the New Model

To evaluate the predictive capability of the new functional form of $W(\alpha_2, \alpha_3)$, the Cauchy stress was found using $W(\alpha_2, \alpha_3)$ and the material constants from **Equation 23** and plugging them into **Equation 7**, which yielded **Equation 26** (Criscione et al. 2002). The deviatoric basis tensors $\mathbf{A_2}$ and $\mathbf{A_3}$ in **Equation 7** were used as defined in Criscione et al. as follows (Criscione et al. 2002):

$$\mathbf{A_2} = \mathbf{e_f} \otimes \mathbf{e_f} - \frac{1}{2}(\mathbf{e_s} \otimes \mathbf{e_s} + \mathbf{e_n} \otimes \mathbf{e_n}) \quad \textbf{(Eq. 24)}$$

$$\mathbf{A_3} = \mathbf{e_n} \otimes \mathbf{e_n} - \mathbf{e_s} \otimes \mathbf{e_s} \quad \textbf{(Eq. 25)}$$

Hence, this yielded

$$\boldsymbol{\sigma}_{\mathbf{QRW}} = \left(\frac{3}{2}\frac{\partial W}{\partial \alpha_2} - \frac{\partial W}{\partial \alpha_3}\right)\mathbf{e_f} \otimes \mathbf{e_f} - 2\frac{\partial W}{\partial \alpha_3}\mathbf{e_s} \otimes \mathbf{e_s} \quad \textbf{(Eq. 26)}$$

To compare it with the Fung model, the Cauchy stress was calculated using the Fung strain energy function $W(E_{ff}, E_{ss}, E_{nn})$ and plugging it into **Equation 3**, yielding **Equations 27a** and **27b**.

$$\sigma_{ff_{Fung}} = \frac{c}{2} e^{Q}\left[b_{ff}{U_{ff}}^{2}({U_{ff}}^{2} - 1) - b_{nn}{U_{nn}}^{2}({U_{nn}}^{2} - 1)\right] \quad \textbf{(Eq. 27a)}$$

$$\sigma_{ss_{Fung}} = \frac{c}{2} e^{Q}\left[b_{ss}{U_{ss}}^{2}({U_{ss}}^{2} - 1) - b_{nn}{U_{nn}}^{2}({U_{nn}}^{2} - 1)\right] \quad \textbf{(Eq. 27b)}$$

where U_{ff}, U_{ss}, and U_{nn} are the diagonal components of the stretch tensor **U** which is found from $\mathbf{U} = \mathbf{C}^{1/2}$. In this experiment, they are equal to λ_1, λ_2, and λ_3, respectively.

It is worth noting that for the Cauchy stress for both models, the pressure was found from the boundary condition of the experiment, $\sigma_{nn} = 0$. Thus, the mathematical form of σ_{nn} for each model was subtracted from both σ_{ff} and σ_{ss} to satisfy the boundary conditions. In addition, the same algorithm that was used to calculate the material constants for $W(\alpha_2, \alpha_3)$ was used to find the material constants c, b_{ff}, b_{ss}, and b_{nn} of the Cauchy stresses of the Fung model by minimizing the squared sum of errors between the experimentally measured and theoretically predicted Fung stresses, shown in **Equation 28**.

$$MSE_{Fung} = \left({\sigma_{ff}}^{pred.} - {\sigma_{ff}}^{meas.}\right)^2 + ({\sigma_{ss}}^{pred.} - {\sigma_{ss}}^{meas.})^2 \quad \textbf{(Eq. 28)}$$

where MSE_{Fung} is the minimized squares of errors of the Cauchy stresses derived from the Fung strain energy function (Appendix A).

To compare the predictive capability of both models, the uncertainty was calculated by summing the squares of errors between the experimental and predicted Cauchy stresses for each model using **Equation 29**.

$$\mathbf{Err}(\boldsymbol{\sigma}) = \sum_{i=1}^{2} \frac{(\sigma_i{}^{pred.} - \sigma_i{}^{meas.})^2}{|\boldsymbol{\sigma}|^2} \qquad \textbf{(Eq. 29)}$$

where $\boldsymbol{\sigma_i}$ represents $\boldsymbol{\sigma_{ff}}$ and $\boldsymbol{\sigma_{ss}}$ for each model, and $|\boldsymbol{\sigma}|^2$ represents the squared magnitude of the experimentally measured Cauchy stress tensor, which is found by contracting the measured Cauchy stress tensor with itself and then subsequently squaring it.

CHAPTER III

RESULTS & DISCUSSION

3.1 Functional Form of $W(\alpha_2, \alpha_3)$

Looking at the dataset in **Figures 6 – 8**, the change in stretch only occurs in the cross-fiber direction (U_{ss}) as the specimen is held constant in the fiber direction at a fixed stretch. As a result, α_2 does not change due to its sole dependency on fiber stretch. Thus, to conclude a functional form of the strain energy function for the data, the relationship between α_3 and $\partial W/\partial \alpha_2$ as well as $\partial W/\partial \alpha_3$ were plotted for loading path only (**Figure 12)**.

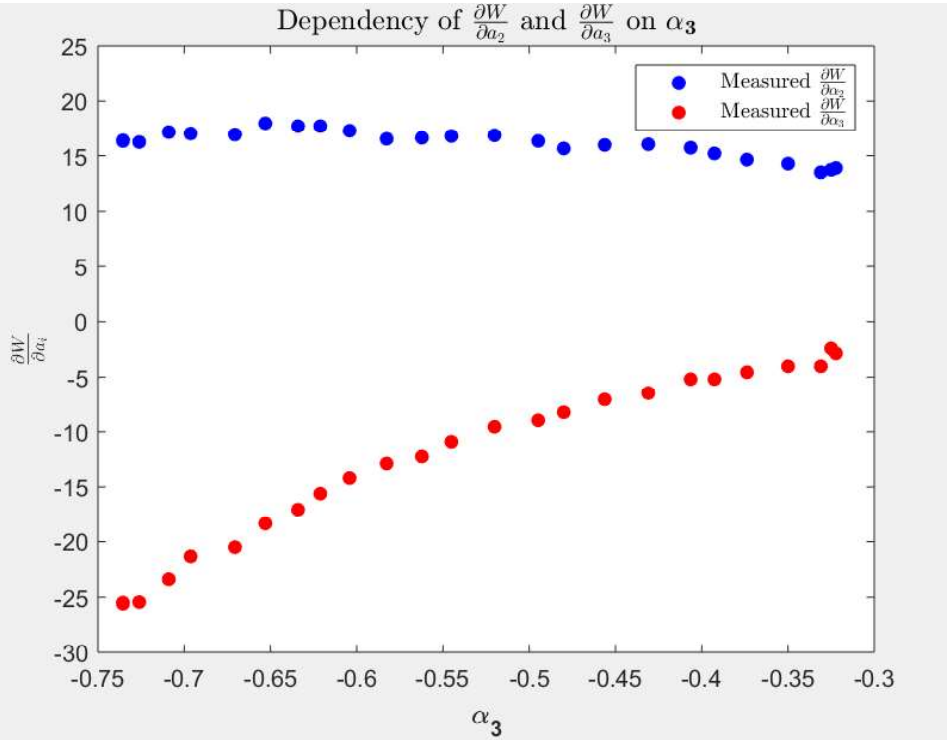

Figure 12. The perturbation of $\partial W/\partial \alpha$ as result of perturbing α_3; the blue dots represent $\partial W/\partial \alpha_2$ whereas the red dots represent $\partial W/\partial \alpha_3$.

From **Figure** 12, it can be observed that there is almost no trend between α_3 and $\partial W/\partial \alpha_2$. It is, therefore, inferred that there is almost no dependency of $\partial W/\partial \alpha_2$ on α_3 when α_2 is constant, and due to the absence of change in α_2 in this experiment, it was inferred that $\partial W/\partial \alpha_2$ is a constant function of α_2. However, considering how $\partial W/\partial \alpha_3$ changes as a function of α_3, there is a clear trend between both variables. Furthermore, the curve fitting tool revealed the relationship to be exponential, with an r-square value of 0.993 (Appendix B). Thus, an exponential fit was the best fit for $\partial W/\partial \alpha_3$. In addition, due to the clear independency of $\partial W/\partial \alpha_2$ of α_3, this implied that $\partial W/\partial \alpha_2$ is a sole function of α_2. Hence, an exponential fit with a similar functional form for $\partial W/\partial \alpha_3$ (using the second dataset) revealed a "good" fit, with an r-square value of 0.996 (Appendix B). Hence, both partial derivatives yielded an exponential function as the best fit for the data. These functional forms are thus:

$$\frac{\partial W}{\partial \alpha_2} = 2\hat{a}_f \hat{b}_f \alpha_2 \mathrm{e}^{\hat{b}_f {\alpha_2}^2} + c_0 \qquad \textbf{(Eq. 30)}$$

$$\frac{\partial W}{\partial \alpha_3} = 2\hat{a}_x \hat{b}_x \alpha_3 \mathrm{e}^{\hat{b}_x {\alpha_3}^2} \qquad \textbf{(Eq. 31)}$$

where $\hat{a_f}$ and $\hat{b_f}$ are fiber material constants, and $\hat{a_x}$ and $\hat{b_x}$ are cross-fiber material constants, and c_0 accounts for adjusting for different slack lengths, which is due to the fact that after pre-conditioning, the zero-stress state is shifted to a new reference. Hence, after integrating each partial derivative, the new form of the strain energy function becomes

$$W(\alpha_2, \alpha_3) = \hat{a}_f \mathrm{e}^{\hat{b}_f {\alpha_2}^2} + \hat{a}_x \mathrm{e}^{\hat{b}_x {\alpha_3}^2} + c_0 \alpha_2 \qquad \textbf{(Eq. 32)}$$

The data interestingly revealed that the strain energy function is separable in two variables, which improves on the Fung model in that its partial derivatives are a function of one variable, minimizing the codependency between both partials. However, in the Fung model, due to the dependency of Q in **Equation 6** on E_{ff}, E_{ss}, and E_{nn}, the partial derivatives of $W(E_{ff}, E_{ss}, E_{nn})$ with respect to each of these Green strains will still contain all the Green strains in the functional forms, which implies more codependency between the individual partials, which may result in a non-ideal fit and a magnified propagation of error (Criscione 2003).

3.2 Material Constants for the New Model

The second dataset (**Figures 9 – 11**) was used to solve for the material constants in **Equations 30 – 32**. Using **Equations 30** and **31**, the material constants that best fit the data and minimizes **Equation 23** are displayed in the following table (**Table 2**):

Table 2. Material constants for the fitted $W(\alpha_2, \alpha_3)$

$\hat{a}_f$	$\hat{b}_f$	$\hat{a}_x$	$\hat{b}_x$	c_0
5.2	5.7	8.9	0.89	– 10

The material constants in **Table 2** demonstrate the amount of energy contributed by each mode of deformation as α_2 and α_3 are perturbed. Furthermore, the values for these constants are consistent with the normal behavior of the heart; the fiber material constants **s**uggest that the increase in strain energy as a result of a perturbation in the fiber stretch (α_2) is greater (roughly by 4-folds) than that of a perturbation in the cross-fiber direction.

This is somewhat consistent with the Frank-Starling mechanism of the heart, which implies that due to a greater increase in the strain energy in the fiber direction, the fibers of the myocardium tend to be relatively more liable to return back to the lower energy state, the resting stretch of the fibers, than if they were stretched in cross-fiber direction. This is also consistent with the fact that during growth adaptations of the heart in response to overcoming greater loads on the heart, the wall of the heart thickens as a result of collective laminar thickening of the fibers, due to stretching in the cross-fiber direction; thus, the heart is able to maintain the state of a thickened wall longer than it would a fiber-stretched state, which perhaps may be due to a higher increase in the strain energy from fiber strains than that of cross-fiber strains. Hence, the material constants in **Table 2** support the physiological observation that myocardial tissue is softer and more compliant in the cross-fiber direction but stiffer in the fiber direction.

3.3 Assessment of the Predictability of the Fung and QR Models

Using the material constants in **Table 2**, the Cauchy stresses predicted by the new model were calculated using **Equation 26** and the strain energy function from **Equation 32**. On the other hand, to calculate the Cauchy stresses predicted by the Fung model, the material constants were first found by finding the best fit that minimizes **Equation 28**. The resulting constants are displayed in **Table 3**. These constants were then plugged in **Equations 27a, b** to find the stresses predicted by the Fung model.

Table 3. Material constants for the fitted Fung model

c	b_{ff}	b_{ss}	b_{nn}
7.4	5.9	2.7	3.8

The plots for the stresses and stress-stretch curves predicted from both models were added to the experimental data plots from **Figures 10** and **11** and were then reproduced in the following figures (**Figures 13 – 16**). The loading path data were used in all the plots.

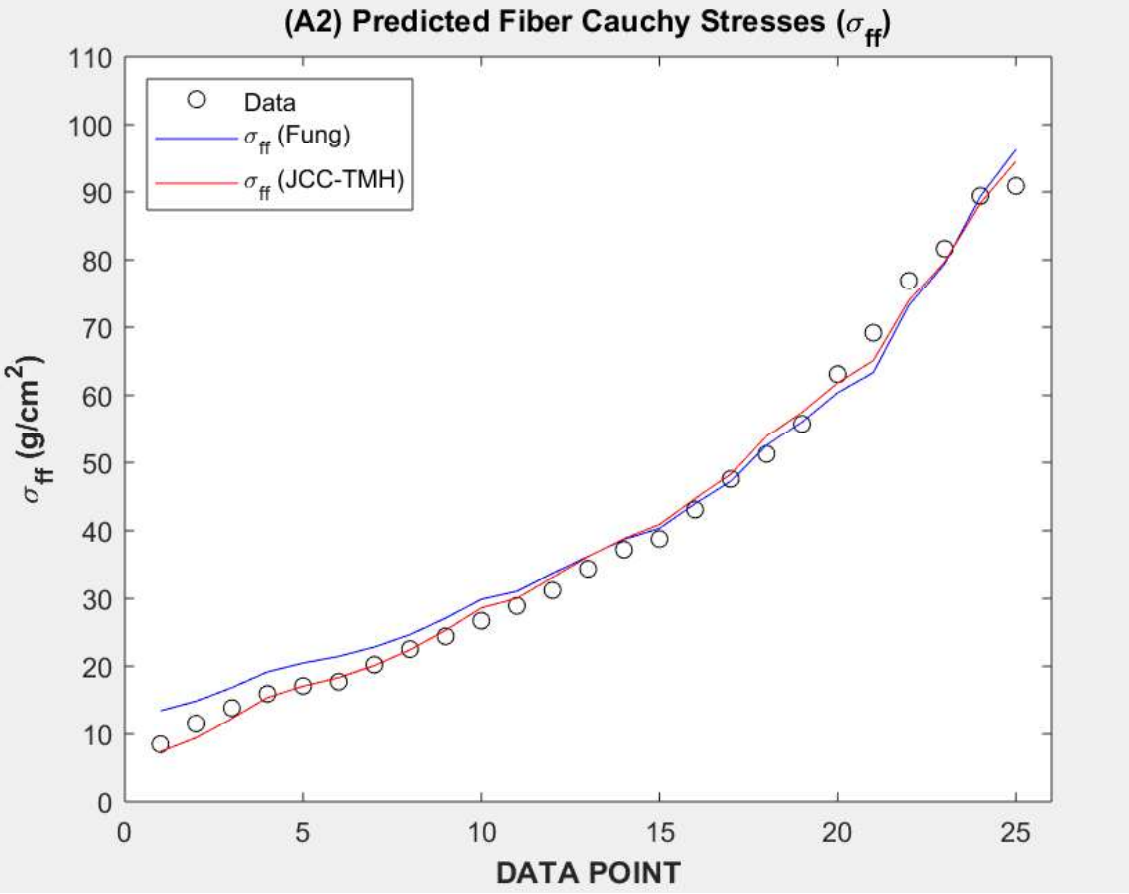

Figure 13. The experimentally measured fiber Cauchy stresses of the loading path (black circles); the predicted stresses from the Fung model (blue line); and the predicted stresses from the QR model (red line)

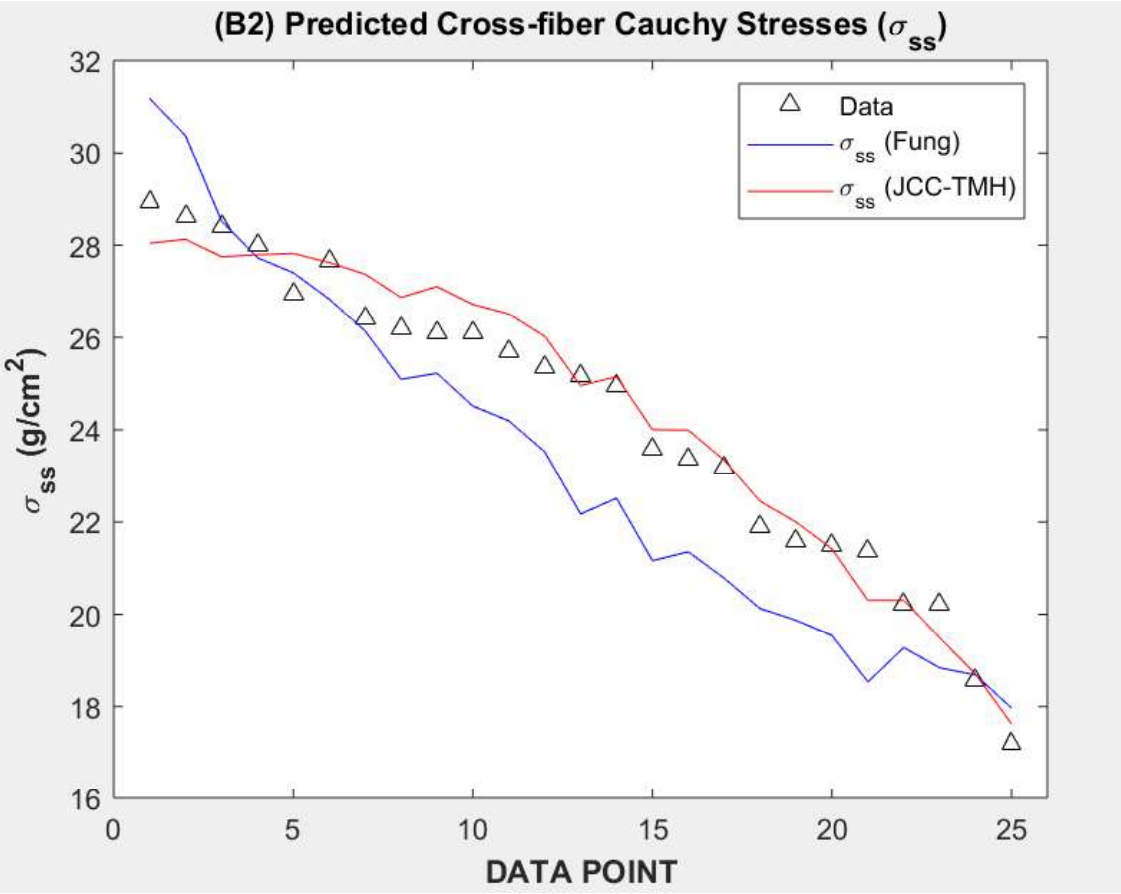

Figure 14. The experimentally measured cross-fiber Cauchy stresses of the loading path (black circles); the predicted stresses from the Fung model (blue line); and the predicted stresses from the QR model (red line)

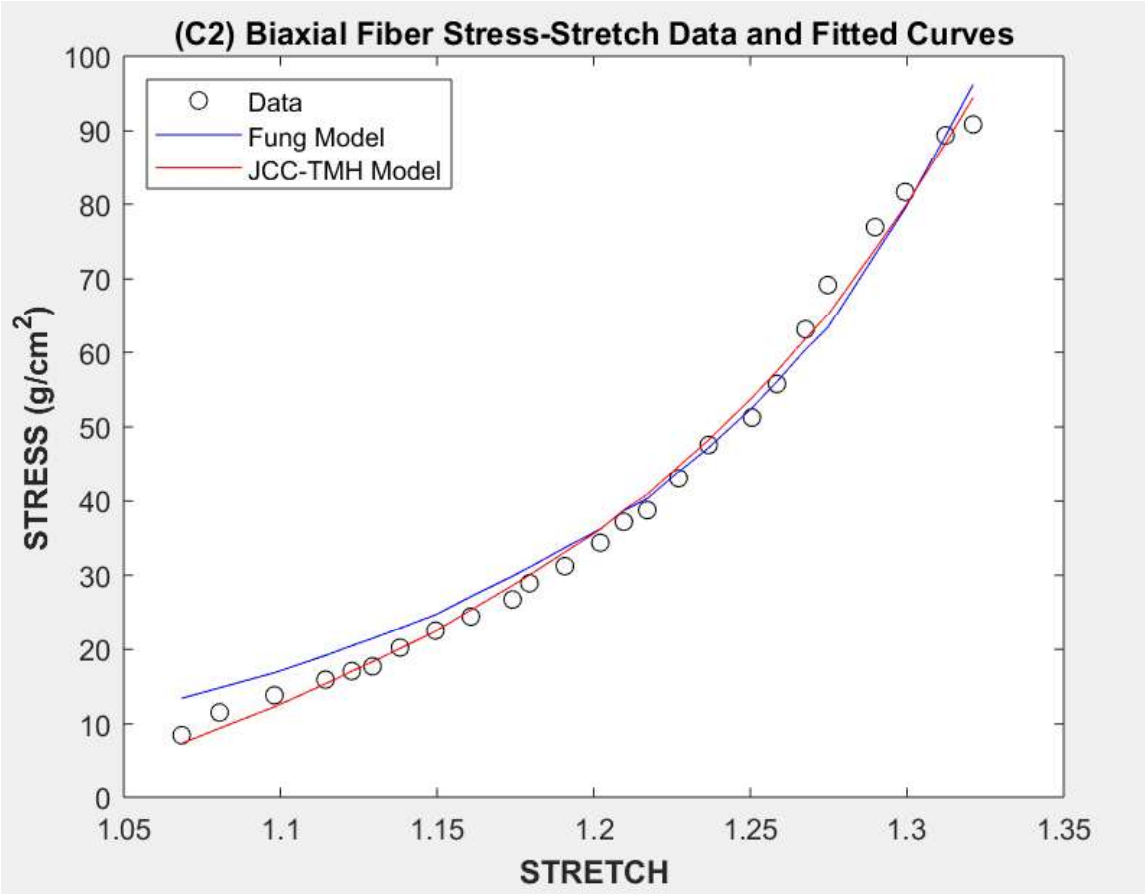

Figure 15. The experimentally measured fiber Cauchy stress-stretch curve of the loading path (black circles); the predicted stress-stretch curve from the Fung model (blue line); and the predicted stress-stretch from the QR model (red line)

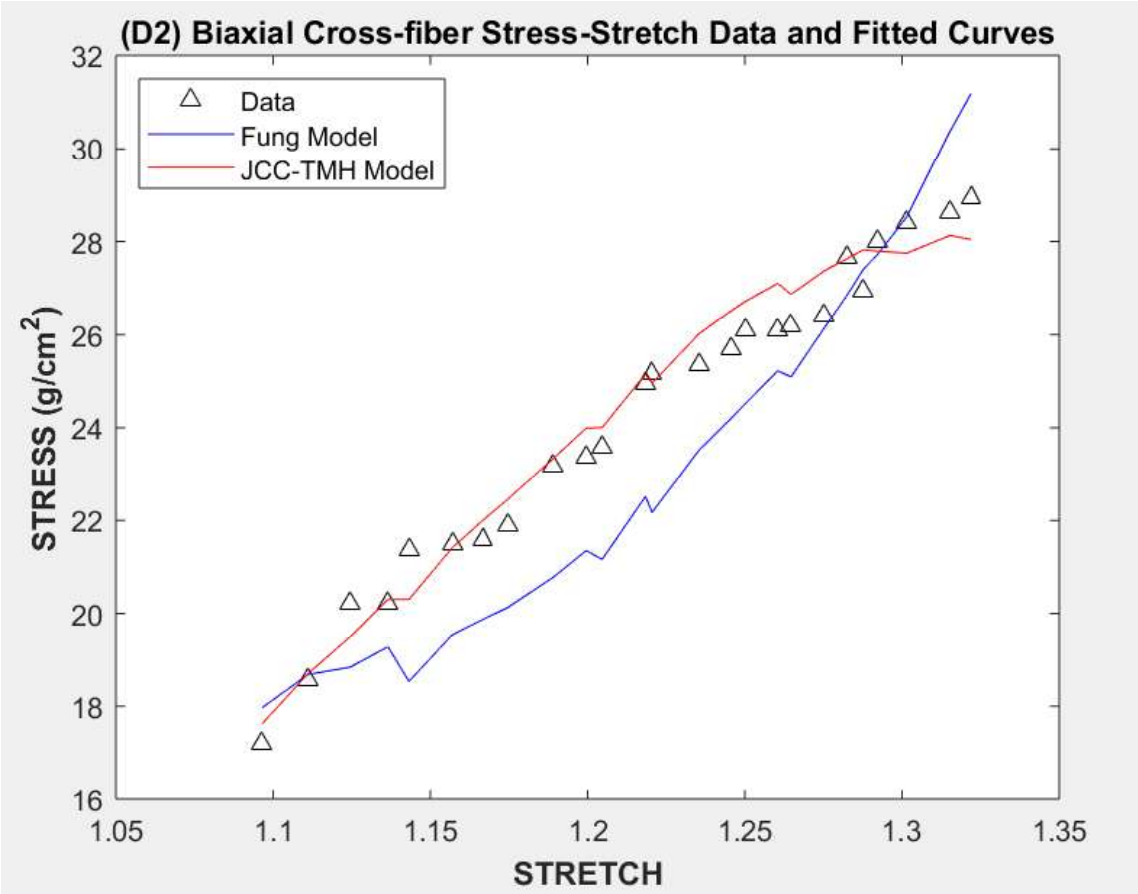

Figure 16. The experimentally measured cross-fiber Cauchy stress-stretch curve of the loading path (black circles); the predicted stress-stretch curve from the Fung model (blue line); and the predicted stress-stretch from the QR model (red line)

3.4 Quantifying the Uncertainty for the Fung and QR Models

Using the predicted stresses obtained from **Equations 26** and **27a, b**, the error was calculated from **Equation 29** to compare with the experimentally measured loading stresses in the second dataset in **Figures 9 – 11**. **Figure 17** shows the plotted uncertainty associated with both models.

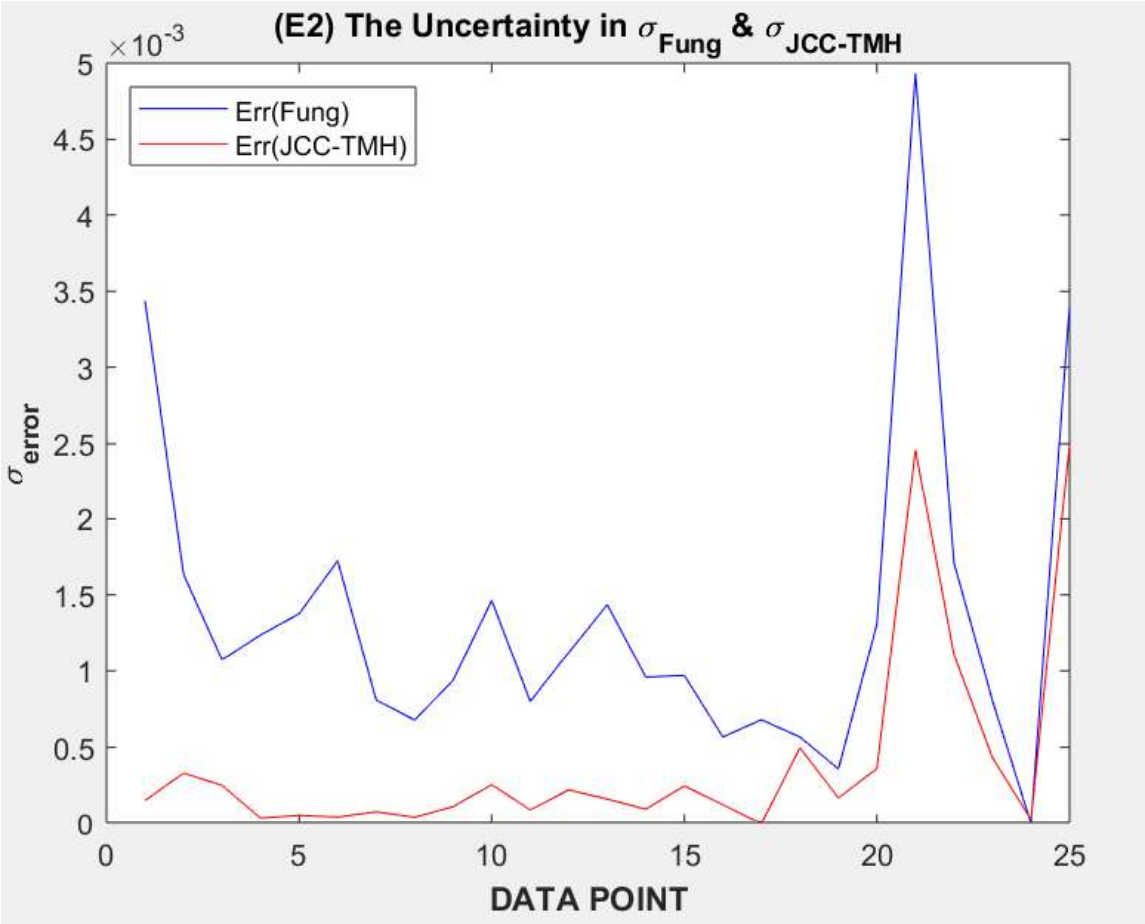

Figure 17. The uncertainty of the Fung model for each data point in the loading path (blue); and the uncertainty of the QR Model for each data point in the loading path (red)

Figure 17 demonstrates a clear reduction in error in the stresses predicted by the QR model compared to that of the Fung model, which indicates the QR model resulted in a better fit for the data. This is due to the fact that the QR model resulted in a strain energy function that is separable in α_2 and α_3 with no codependency between the partial derivatives. However, there was significant codependency between the $\partial W/\partial E_{ii}$ terms of the Fung model as result of the presence of the exponent Q, a function of (E_{ff}, E_{ss}, E_{nn}), in the mathematical expression for each individual term. Additionally, when fitting biaxial

data, the two equations (**Equation 30** and **31**) were controlled by two variables whereas the two equations **(Equations 27a, b**) from the Fung model were controlled by three variables (E_{ff}, E_{ss}, E_{nn}) which results in a greater degeneracy of the possible solutions that fit the data, and decreases the probability of obtaining the "correct" fit. That is, the fit that uniquely characterizes the mechanical behavior of the myocardium and accurately predicts its mechanics.

Therefore, it is concluded from the data that a strain energy function that is separable in its variables yields a better fit and a greater reduction in error than a strain energy function that is not. Furthermore, the QR model yields a strain energy function with less degeneracy and thus a greater probability of uniqueness. Finally, the QR strain energy function carries direct physical meaning regarding cardiac deformation compared to the that of the Fung model.

CHAPTER IV

FUTURE WORK: FINDING THE FULL FORM OF *W* FROM TRIAXIAL TESTING

4.1 Introduction

While QR decomposition provided the foundation for deriving a new strain energy function from biaxial data, biaxial testing is limited in the information it provides about the mechanics of the heart. Biaxial data allowed the strain energy function to be quantified with respect to two modes of deformation (α_2 and α_3); however, a true survey of the mechanics of the heart with the assumption of incompressibility would also include the three other modes of deformation, namely the modes representing simple shear, which are α_4, α_5, and α_6. Therefore, it is of interest to investigate triaxial data, such as that published by Li et al. (Li et al. 2020). Such an investigation will result into a full quantification of the strain energy function and a thorough comparison between the Fung model (**Equation 33**) and the QR model (**Equation 34**) in their full forms.

$$W = W(E_{ff}, E_{ss}, E_{nn}, E_{fs}, E_{fn}, E_{sn}) \quad \textbf{(Eq. 33)}$$

$$W = W(\alpha_2, \alpha_3, \alpha_4, \alpha_5, \alpha_6) \quad \textbf{(Eq. 34)}$$

4.2 Optimal Triaxial Testing Data

Optimal triaxial data was obtained and published from multi-axial testing of a cubic specimen of myocardium with dimensions 1cm × 1cm × 1cm (Avazmohammadi et

al. 2018; Li et al. 2020). Furthermore, Avazmohammadi et al. developed a triaxial apparatus that can determine the optimal combination of possible loading paths (i.e., the optimal experimental design (OED)) that minimizes the uncertainty in the material parameters estimated from the constitutive model (Avazmohammadi et al. 2018).

The specimen used in Li et al. was a cubic specimen whose edges aligned with the anatomical directions of the left ventricle: longitudinal (from base to apex), circumferential, and radial (from endocardium to epicardium). The set of loading paths that minimizes the covariance between the material parameters and optimizes their estimation through maximizing the information potentially obtained from these parameters is a combination of one-axis simple shear and two-axis pure shear deformations (Li et al. 2020). Hence, these optimal loading paths were determined based on the constitutive model utilized by Li et al., which is an invariant-based constitutive form proposed by Holzapfel and Ogden (Holzapfel and Ogden 2009). The following figures (**Figures 18 & 19**) demonstrate the mechanical testing apparatus and the optimal loading paths (i.e., "optimal triaxial") used for the myocardial specimen.

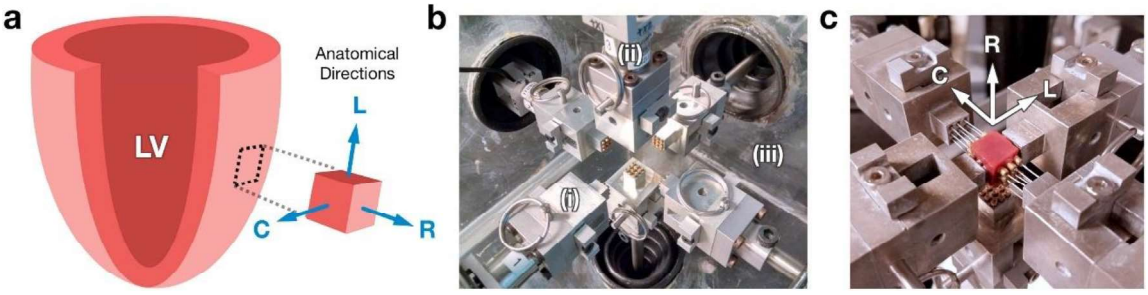

Figure 18. (a) Tissue specimen alignment with respect to the anatomical directions of the heart. (b) Triaxial mechanical testing device (c) Myocardium specimen mounted with anatomical directions aligned to the device axes. Reprinted from (Li et al. 2020)

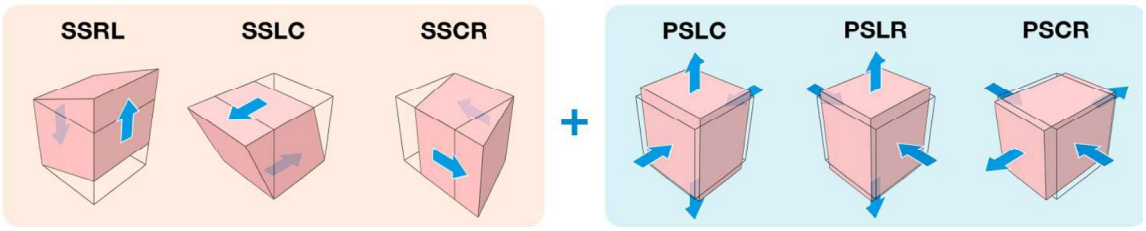

Figure 19. "Optimal Triaxial" loading paths applied to a cuboidal myocardium specimen with edges aligned to the anatomical directions of the heart with the reference configuration shown by the black outline. Reprinted from (Li et al. 2020).

Figure 19 shows the six modes of deformation and the possible stretch directions encoded in the six components of the upper triangular tensor (**Equation 14**), where the first three deformations (SSRL, SSLC, and SSCR) represent simple shear of the radial plane along the longitudinal axis, simple shear of the longitudinal plane along the circumferential axis, and simple shear of the circumferential plane along the radial axis, respectively. These simple shear deformations correspond to α_4, α_5, and α_6, respectively, after applying a coordinate transformation from lab coordinates to material coordinates. Furthermore, the latter three deformations (PSLC, PSLR, and PSCR) represent pure shear (i.e., stretch) along the longitudinal axis and shortening along the circumferential axis, pure shear in the longitudinal axis and shortening along the radial axis, and pure shear along the circumferential axis with shortening along the radial axis, respectively. These pure shear deformations are encoded in α_2 and α_3, allowing the full form of the strain energy function $W(\alpha_2, \alpha_3, \alpha_4, \alpha_5, \alpha_6)$ to be derived by using the triaxial data to find functional forms for $\partial W/\partial\alpha_2$, $\partial W/\partial\alpha_3$, $\partial W/\partial\alpha_4$, $\partial W/\partial\alpha_5$, and $\partial W/\partial\alpha_6$ using their respective equations in Criscione et al. (Criscione et al. 2002).

4.3 Limitations

The limitations in this study mainly stem from the fact that the multiaxial testing is conducted on a myocardial cube. While that does allow for decoding the behavior with more modes of deformation than that allowed by biaxial testing, the heterogeneity of the cube makes finding the material constants that truly characterizes the cube less unique. Furthermore, the cube can be thought of as a sum of slabs stacked upon each other, with each slab having a unique fiber direction, so the behavior would have to be averaged across the slabs to enable finding the material constants that represents this average behavior. Such a limitation should, thus, be kept in mind while analyzing the triaxial data.

4.4 Conclusion

The aforementioned published optimal triaxial data of a myocardial cuboid can be used to derive the full functional form and material constant estimation for **Equation 33** (Li et al. 2020). The resulting function can then be compared with the Fung model using the same theoretical framework in the thesis, which can be extended for triaxial testing.

CHAPTER V

CONCLUDING REMARKS & CHALLENGES OF MODELING CARDIAC MECHANICS

5.1 Conclusion

Published biaxial data for a slab specimen of myocardium was utilized to find a strain energy function from QR decomposition (Humphrey et al. 1990). The goal of this work was to improve on the Fung model by deriving a strain energy function that yielded better stress-stretch fits (thus greater predictive capabilities), and utilizes strain parameters that relate more physically with the deformation of the heart. Indeed, the proposed strain energy function in **Equation 32** achieves just that, and it also has less codependency amongst its partial derivatives, reducing the propagated error. Hence, this minimizes the degeneracy of the model and improves significantly on the Fung model for the strain energy function, which allows linking the new model to the multiscale structure of the heart more achievable.

5.2 The Path That Lies Ahead

While the fruits of this work might be considered a great step forward in improving the mathematical models of the heart, it is but one step. There is, therefore, ample room for improvement, and modeling the heart in of itself is a field that is inherent with many complexities, stemming from the fact that is both a mechanical and biological system. Regarding its mechanics, due to its nature described in **1.5**, a better model for its elasticity

would be a viscoelastic model compared to the framework of hyperelasticity assumed in this work. Unfortunately, the mechanics of viscoelasticity is currently not well-established. Furthermore, due to the heterogeneity of the heart, a better model is that factors cardiac anisotropy given that different regions of the heart behave in different manners. Also, while this work was done for the passive myocardium, which corresponds to a non-contractile heart, a more realistic model for the heart would be that which is active, opening the door for far more variables to be included.

Another possible avenue for improvement concerns the methods that generate the constitutive relations by simply "fitting the data". Furthermore, the solution found is often not "the" solution simply because it fits the data, for there are often models that "fit" the data but are clearly not representative of the natural phenomenon. To illustrate, prior to the advent of Newton's second law ($\vec{F} = m\vec{a}$), it might have been easy to assume a geocentric model for the universe, by observing the "motion" of the Sun in the sky. While it "fits" the observation that the Sun is "moving" in the sky around Earth, it does not capture the reality of nature. However, with Newton's second and third laws, there are restrictions put by how much the Sun can accelerate relative to Earth due to its great mass. This implies that Earth must accelerate relatively greater as its mass is lower, so that the forces of gravitational attraction between the Sun and the Earth are equal and opposite, as predicted by Newton's third law. Another example is that of a chariot model pulling on the Moon along its orbit, which "fits" the observation of the motion of the Moon around the Earth. While the true model is the gravitationally distorted space-time within Earth's

vicinity that yields the force pulling on the Moon towards its center, the chariot model was just "off" in its direction of pull by 90 degrees.

These examples demonstrate why deriving models with low degeneracy is an endeavor that is of utmost importance in the field of cardiac mechanics, to ensure a higher probability of yielding the true model as opposed a model that merely "fits". Nonetheless, it is possible that numerical methods may not be the best framework to yields such models, and it is possible that other methods, such as perturbation theory or even other methods that have yet to be invented, would be more ideal to model the heart.

Finally, the true complexity of modeling the mechanics of the hearts lie in that it is a biological system that harbors life, and thus varies with age, medical history, size, genetic predispositions, …etc. This is, indeed, the ultimate complexity of the heart, and such a complexity may have yet to be encountered by other fields of mechanics. For instance, all of the models and equations describing the Universe are based on experiments and observations of one Universe, the universe where Earth resides. For the sake of argument, while it has not been experimentally proven yet, let us assume that the multiverse is indeed the true model of nature. According to string theory, the multiverse would be comprised of 10^{500} universes, yet let us assume that it is made up of seven billion universes, as an example. This implies that while Newton's second law is $\vec{F} = m\vec{a}$ in universe 1, it could be represented completely differently, such as $\vec{F} = \frac{1}{b} Fred \times Velma$ in universe 2. Universe 3 would have a different expression, and so forth. As a result, there would be seven billion different expressions for force. If there were to be an overarching expression that encompasses and unifies all seven billion expressions, such a unification

will most likely require a highly advanced level of mathematics, or possibly another tool, that has not been developed and would thus encompass multiple layers of complexity.

While this dilemma is not yet present in astrophysics, it is for cardiac mechanics. Furthermore, there are indeed roughly seven billion human hearts on Earth, each one beating differently than the other with great biological variability. Even within the same individual's lifetime, the behavior of the heart varies with time. Hence, obtaining such an overarching model for the heart poses a great challenge, yet it is not out of reach.

Nevertheless, a unique aspect of cardiac mechanics modeling is that it involves a structure that humans use every day and would want preserved for as long as possible. Hence, another aspect of modeling for the heart that must be kept in mind is not just the "exactness" of the model, but also to what degree is the exactness deemed "appropriate". That question can be answered by considering the application for which the model will be used. For instance, while a flat earth is an ill-conceived model to measure Earth's gravitational field, it is quite a sufficient model for constructing street maps. Likewise, an oblate ellipsoidal model may be truer to Earth's geometry, yet assuming it to be a sphere is sufficient for estimating the force of gravitation using Newton's universal law of gravitation, to an acceptable degree of certainty.

REFERENCES

Avazmohammadi R, Li DS, Leahy T, et al (2018) An integrated inverse model-experimental approach to determine soft tissue three-dimensional constitutive parameters: Application to post-infarcted myocardium. Biomech Model Mechanobiol 17:31–53. https://doi.org/10.1007/s10237-017-0943-1

Costa KD, Takayama Y, McCulloch AD, Covell JW (1999) Laminar fiber architecture and three-dimensional systolic mechanics in canine ventricular myocardium. Am J Physiol - Hear Circ Physiol 276:. https://doi.org/10.1152/ajpheart.1999.276.2.h595

Criscione JC (1999) Development of a Finite Hyperelasticity Theory for Transversely Isotropic Material Behavior with Subsequent Analysis of Mechanical Tests on Myocardium. Doctoral dissertation, The Johns Hopkins University

Criscione JC (2003) Rivlin's representation formula is ill-conceived for the determination of response functions via biaxial testing. J Elast 70:129–147. https://doi.org/10.1023/B:ELAS.0000005586.01024.95

Criscione JC (2011) On Modeling the Mechanical Behavior of Matter : The Continuum Assumption. IJSCS 3:55–59

Criscione JC, McCulloch AD, Hunter WC (2002) Constitutive framework optimized for myocardium and other high-strain, laminar materials with one fiber family. J Mech Phys Solids 50:1681–1702. https://doi.org/10.1016/S0022-5096(01)00138-7

Fung YC (1967) Elasticity of soft tissues in simple elongation. Am J Physiol 213:1532–1544. https://doi.org/10.1152/ajplegacy.1967.213.6.1532

Fung YC (1983) On the foundations of biomechanics. ASME J Appl Mech 50:1003–1009. https://doi.org/10.1093/bjps/XV.57.1

Fung YC (1990) Biomechanics: Motion, Flow, Stress, and Growth. Springer

Fung YC (1993) Biomechanics: Mechanical properties of living tissues. Springer

Fung YC (1995) Stress, Strain, growth, and remodeling of living organisms. Z Angew Math Phys 46:S469-482. https://doi.org/10.1007/978-3-0348-9229-2

Fung YC (1973) Biorheology of Soft Tissues. Biorheology 10:139–155

Holzapfel GA, Ogden RW (2009) Constitutive modelling of passive myocardium: A structurally based framework for material characterization. Philos Trans R Soc A Math Phys Eng Sci 367:3445–3475. https://doi.org/10.1098/rsta.2009.0091

Humphrey JD (2003) Continuum biomechanics of soft biological tissues. Proc. R. Soc. A Math. Phys. Eng. Sci. 459:3–46

Humphrey JD (2002) Cardiovascular Solid Mechanics: cells, tissues, and organs. Springer

Humphrey JD, Strumpf RK, Yin FCP (1990) Determination of a constitutive relation for passive myocardium: I. - A New Functional Form. J Biomech Eng 112:333–3339. https://doi.org/10.1115/1.2891194

Humphrey JD, Yin FCP (1989) Biomechanical experiments on excised myocardium: Theoretical considerations. J Biomech 22:377–383. https://doi.org/10.1016/0021-9290(89)90052-3

Li DS, Avazmohammadi R, Merchant SS, et al (2020) Insights into the passive mechanical behavior of left ventricular myocardium using a robust constitutive model based on full 3D kinematics. J Mech Behav Biomed Mater 103:. https://doi.org/10.1016/j.jmbbm.2019.103508

Martin RB (1999) A Genealogy of Biomechanics. 23rd Annual Conference of the American Society of Biomechanics. University of Pittsburgh, Pittsburgh PA. Presidential Lecture

Srinivasa AR (2012) On the use of the upper triangular (or QR) decomposition for developing constitutive equations for Green-elastic materials. Int J Eng Sci 60:1–12. https://doi.org/10.1016/j.ijengsci.2012.05.003

APPENDIX A

ANNOTATED MATLAB CODES

The algorithms in the following sections were all written in MATLAB R2018a.

A.1 Biaxial Data Plotter Program

```
close all; clear all; clc
% Plotting the Data from Humphrey et. al (1990)

% First Data Set

% [x,U_ff] = DataThief('STRETCH.JPG',[0 1.4],[0 1],[50 0]);
% [x,U_ss] = DataThief('STRETCH.JPG',[0 1.4],[0 1],[50 0]);
% [x,sigma_ff] = DataThief('STRESS.JPG',[0 100],[0 0],[50 0]);
% [x,sigma_ss] = DataThief('STRESS.JPG',[0 100],[0 0],[50 0]);

% Stretch (Constant Fiber Stretch & Varying Cross-fiber Stretch)
U_ff1 = [1.2010    1.1986    1.1981    1.1981    1.1986    1.2006
      1.2010    1.2006    1.2006    1.2006    1.1998    1.1998
      1.1998    1.2006    1.2006    1.1998    1.2010    1.1998...
      1.2006    1.2006    1.2006    1.2006    1.2006    1.2006
      1.2006    1.2006    1.2019    1.2010    1.2010    1.2010
      1.2010    1.2010    1.2010    1.2010    1.2010    1.2010...
      1.1998    1.2006    1.2006    1.2006    1.1998    1.2006
      1.1998    1.2006    1.2010    1.2010    1.2031    1.2035
      1.2035    1.1986];

U_ss1 = [1.0735    1.0731    1.0780    1.0883    1.1011    1.1106
      1.1181    1.1321    1.1465    1.1602    1.1692    1.1841
      1.1990    1.2089    1.2213    1.2349    1.2448    1.2535...
      1.2650    1.2762    1.2927    1.3009    1.3121    1.3183
      1.3183    1.3187    1.3030    1.2939    1.2815    1.2704
      1.2605    1.2535    1.2411    1.2312    1.2213    1.2138...
      1.1977    1.1891    1.1792    1.1692    1.1593    1.1544
      1.1391    1.1255    1.1218    1.1102    1.1011    1.0970
      1.0888    1.0743];

% Cauchy Stress
sigma_ff1 = [22.9941   23.6791   24.2661   25.4403   26.5166
      27.9843   28.7671   30.5284   31.0176   31.7025   33.4638
      34.8337   36.1057   37.1820   37.6712   40.1174   42.1722
      43.6399...
```

```
      45.3033   45.8904   46.8689   49.1194   49.8043   50.0978
      50.0978   48.0431   43.6399   42.4658   41.8787   40.0196
      39.5303   37.7691   37.9648   36.3992   35.4207   33.3659...
      31.1155   30.6262   30.5284   29.8434   29.7456   29.7456
      28.1800   26.8102   26.7123   26.9080   26.9080   26.2231
      24.5597   22.6027];

sigma_ss1 = [4.7945    5.6751    8.0235    8.0235    9.0998
      10.3718   10.3718   12.9159   14.0900   16.4384   17.9061
      19.0802   21.8200   24.4618   25.7339   28.3757   31.2133...
      34.1487   36.6928   40.9980   42.6614   46.7710   50.8806
      51.1742   50.9785   48.6301   40.6067   36.3014   33.4638
      30.8219   26.9080   26.6145   23.7769   21.0372...
      18.6888   18.5910   16.0470   13.4051   13.4051   13.3072
      12.1331   10.9589    9.7847    9.7847    9.4912    8.5127
      7.0450    7.0450    5.9687    4.9902];

% Plotting Loading Data from the First Data Set
    U_ff1 = U_ff1(1:25);
    U_ss1 = U_ss1(1:25);
    sigma_ff1 = sigma_ff1(1:25);
    sigma_ss1 = sigma_ss1(1:25);

% Humphrey Plots

figure (1)  % STRETCH
     plot(U_ff1,'o'); hold on; plot(U_ss1,'r^'); axis([0 50 1
     1.4]);
     title('(A) Measured Fiber and Cross-fiber Stretches
     \bf{U_{ff}, U_{ss}}');
     xlabel('DATA POINT','fontweight','bold');
     ylabel('STRETCH','fontweight','bold');
     legend('U_{ff}','U_{ss}')

figure (2)  % STRESS
    plot(sigma_ff1,'o'); hold on; plot(sigma_ss1,'r^'); axis([0 50
    0 100]);
    title('(B) Measured Fiber and Cross-fiber Stretches
    \bf{\sigma_{ff}, \sigma_{ss}}');
    xlabel('DATA POINT','fontweight','bold'); ylabel('STRESS
    (g/cm^{2})','fontweight','bold');
    legend('\sigma_{ff}','\sigma_{ss}')

figure(3)  % STRETCH-STRESS
    plot(U_ff1,sigma_ff1,'o'); hold on; plot(U_ss1,sigma_ss1,'r^');
    axis([1 1.4 0 100 ]);
    title('(C) Biaxial Fiber and Cross-fiber Stress-Stretch Data');
    xlabel('STRETCH','fontweight','bold'); ylabel('STRESS
    (g/cm^{2})','fontweight','bold');
    legend('fiber','cross-fiber')
```

```
% Second Data Set

% [x,U_ff] = DataThief('STRETCH2.JPG',[0 1.4],[0 1],[50 0]);
% [x,U_ss] = DataThief('STRETCH2.JPG',[0 1.4],[0 1],[50 0]);
% [x,sigma_ff] = DataThief('STRESS2.JPG',[0 100],[0 0],[50 0]);
% [x,sigma_ss] = DataThief('STRESS2.JPG',[0 100],[0 0],[50 0]);

% Stretch (Varying Fiber Stretch & Varying Cross-fiber Stretch)
U_ff2 = [1.0685    1.0806    1.0981    1.1144    1.1228    1.1294
      1.1382    1.1495    1.1608    1.1741    1.1795    1.1908
      1.2021    1.2096    1.2171    1.2271    1.2367    1.2505...
      1.2585    1.2676    1.2747    1.2898    1.2994    1.3123
      1.3211    1.3219    1.3219    1.3119    1.2973    1.2881
      1.2756    1.2635    1.2518    1.2468    1.2347    1.2271...
      1.2121    1.2046    1.1933    1.1808    1.1695    1.1595
      1.1541    1.1445    1.1353    1.1232    1.1106    1.1044
      1.0944    1.0739];

U_ss2 = [1.3219    1.3152    1.3015    1.2923    1.2877    1.2823
      1.2752    1.2647    1.2605    1.2501    1.2455    1.2355
      1.2205    1.2184    1.2046    1.1996    1.1891...
      1.1745    1.1666    1.1570    1.1432    1.1365    1.1244
      1.1111    1.0965    1.0860    1.0856    1.0864    1.0931
      1.1061    1.1190    1.1357    1.1520    1.1645...
      1.1758    1.1883    1.2017    1.2129    1.2259    1.2317
      1.2480    1.2555    1.2605    1.2651    1.2781    1.2843
      1.2952    1.3027    1.3111    1.3278];


% Cauchy Stress
sigma_ff2 = [8.4906   11.5304   13.8365   15.9329   17.0860
      17.7149   20.2306   22.5367   24.4235   26.7296   28.9308
      31.2369   34.3816   37.2117   38.7841   43.0818   47.5891
      51.2579...
      55.7652   63.1027   69.1824   76.9392   81.6562   89.4130
      90.8805   90.8805   81.9706   66.1426   54.8218   49.1614
      43.1866   37.8407   35.3249   33.6478   31.5514   29.0356...
      25.9958   24.5283   21.5933   20.1258   18.6583   18.5535
      16.6667   16.0377   14.3606   12.7883   12.1593   11.3208
      10.2725    8.1761];

sigma_ss2 = [28.9308   28.6164   28.4067   27.9874   26.9392
      27.6730   26.4151   26.2055   26.1006   26.1006   25.6813
      25.3669   25.1572   24.9476   23.5849   23.3753   23.1656...
      21.9078   21.5933   21.4885   21.3836   20.2306   20.2306
      18.5535   17.1908   16.2474   14.9895   14.8847   14.8847
      14.9895   15.1992   16.6667   17.8197   19.2872...
```

```
      20.6499   21.0692   22.4319   22.8512   23.6897   24.2138
      24.3187   25.6813   25.7862   25.7862   26.2055   28.0922
      27.8826   29.2453   29.2453   30.9224];

% Plotting Loading Data from the Second Data Set
    U_ff2 = U_ff2(1:25);
    U_ss2 = U_ss2(1:25);
    sigma_ff2 = sigma_ff2(1:25);
    sigma_ss2 = sigma_ss2(1:25);

% Humphrey Plots

figure (4)  % STRETCH
    plot(U_ff2,'o'); hold on; plot(U_ss2,'r^'); axis([0 50 1 1.4]);
    title('(D) Measured Fiber and Cross-fiber Stretches \bf{U_{ff},
    U_{ss}}');
    xlabel('DATA POINT','fontweight','bold');
    ylabel('STRETCH','fontweight','bold');
    legend('U_{ff}','U_{ss}')

figure (5)  % STRESS
    plot(sigma_ff2,'o'); hold on; plot(sigma_ss2,'r^'); axis([0 50
    0 100]);
    title('(E) Measured Fiber and Cross-fiber Stretches
    \bf{\sigma_{ff}, \sigma_{ss}}');
    xlabel('DATA POINT','fontweight','bold'); ylabel('STRESS
    (g/cm^{2})','fontweight','bold');
    legend('\sigma_{ff}','\sigma_{ss}')

figure(6)  % STRETCH-STRESS
    plot(U_ff2,sigma_ff2,'o'); hold on; plot(U_ss2,sigma_ss2,'r^');
    axis([1 1.4 0 100 ]);
    title('(F) Biaxial Fiber and Cross-fiber Stress-Stretch Data');
    xlabel('STRETCH','fontweight','bold'); ylabel('STRESS
    (g/cm^{2})','fontweight','bold');
    legend('fiber','cross-fiber')
```

A.2 Computation of the Kinematics

```
% Enforcing the Incompressibility Constraint
    for i = 1:length(U_ff1)
        U_nn1(i) = 1/(U_ff1(i)*U_ss1(i));
        U_nn2(i) = 1/(U_ff2(i)*U_ss2(i));
    end

% Finding the Green Strains
    for i = 1:length(U_ff1)
        E_ff1(i) = 0.5*(U_ff1(i)^2 - 1);
        E_ss1(i) = 0.5*(U_ss1(i)^2 - 1);
        E_nn1(i) = 0.5*(U_nn1(i)^2 - 1);
        E_ff2(i) = 0.5*(U_ff2(i)^2 - 1);
        E_ss2(i) = 0.5*(U_ss2(i)^2 - 1);
        E_nn2(i) = 0.5*(U_nn2(i)^2 - 1);
    end

E_fs1 = zeros(1,50); E_fn1 = zeros(1,50); E_sn1 = zeros(1,50);
E_fs2 = zeros(1,50); E_fn2 = zeros(1,50); E_sn2 = zeros(1,50);

% Components of the f Tensor (1)
    for i = 1:length(E_ff1)
        f_ff1(i) = sqrt(2*E_ff1(i)+1);
        f_fs1(i) = (2*E_fs1(i))/f_ff1(i);
        f_fn1(i) = (2*E_fn1(i))/f_ff1(i);
        f_ss1(i) = sqrt(2*E_ss1(i) - f_fs1(i)^2 + 1);
        f_sn1(i) = (2*E_sn1(i) - f_fs1(i)*f_fn1(i))/f_ss1(i);
        f_nn1(i) = sqrt(2*E_nn1(i) - (f_fn1(i)^2 + f_fs1(i)^2)+ 1);
        f1(:,:,i) = [f_ff1(i) f_fs1(i) f_fn1(i); 0 f_ss1(i)
        f_sn1(i); 0 0 f_nn1(i)];
        f_trans1(:,:,i) = f1(:,:,i).';
    end

% Components of the f Tensor (2)
    for i = 1:length(E_ff1)
        f_ff2(i) = sqrt(2*E_ff2(i)+1);
        f_fs2(i) = (2*E_fs2(i))/f_ff2(i);
        f_fn2(i) = (2*E_fn2(i))/f_ff2(i);
        f_ss2(i) = sqrt(2*E_ss2(i) - f_fs2(i)^2 + 1);
        f_sn2(i) = (2*E_sn2(i) - f_fs2(i)*f_fn2(i))/f_ss2(i);
        f_nn2(i) = sqrt(2*E_nn2(i) - (f_fn2(i)^2 + f_fs2(i)^2)+ 1);
        f2(:,:,i) = [f_ff2(i) f_fs2(i) f_fn2(i); 0 f_ss2(i)
        f_sn2(i); 0 0 f_nn2(i)];
        f_trans2(:,:,i) = f2(:,:,i).';
    end
```

```
% Kinematic Variables (1)

    for i=1:length(E_ff1)
        lambda_f1(i) = f_ff1(i);
        zeta1(i) = ((lambda_f1(i))^0.5)*f_nn1(i);
        phi_fs1(i) = ((lambda_f1(i))^-1)*f_fs1(i);
        phi_fn1(i) = ((lambda_f1(i))^-1)*f_fn1(i);
        phi_sn1(i) = ((lambda_f1(i))^0.5)*zeta1(i)*f_sn1(i);
    end

% Kinematic Variables (2)

    for i=1:length(E_ff1)
        lambda_f2(i) = f_ff2(i);
        zeta2(i) = ((lambda_f2(i))^0.5)*f_nn2(i);
        phi_fs2(i) = ((lambda_f2(i))^-1)*f_fs2(i);
        phi_fn2(i) = ((lambda_f2(i))^-1)*f_fn2(i);
        phi_sn2(i) = ((lambda_f2(i))^0.5)*zeta2(i)*f_sn2(i);
    end

% Strain parameters (1)

    for i=1:length(E_ff1)
        a2_1(i) = 1.5*log(lambda_f1(i));
        a3_1(i) = 2*log(zeta1(i));
        a4_1(i) = phi_fs1(i);
        a5_1(i) = phi_fn1(i);
        a6_1(i) = phi_sn1(i);
    end

% Strain parameters (2)

    for i=1:length(E_ff1)
        a2_2(i) = 1.5*log(lambda_f2(i));
        a3_2(i) = 2*log(zeta2(i));
        a4_2(i) = phi_fs2(i);
        a5_2(i) = phi_fn2(i);
        a6_2(i) = phi_sn2(i);
    end
```

A.3 Parameter Estimation for Both Models

```
%% FUNG MODEL

% Fung Cauchy Stress (Sigma)

    U_1 = [U_ff1;U_ss1;U_nn1;E_ff1;E_ss1;E_nn1];
    U_2 = [U_ff2;U_ss2;U_nn2;E_ff2;E_ss2;E_nn2];
    U = [U_1;U_2];

% (1)

    tff_Fung1 = @(b,U)0.5.*b(1).*exp(b(2).*E_ff1.^2 +
          b(3).*E_ss1.^2 +
          b(4).*E_nn1.^2).*(b(2).*U_ff1.^2.*(U_ff1.^2 - 1) -
          b(4).*U_nn1.^2.*(U_nn1.^2-1));

    tss_Fung1 = @(b,U)0.5.*b(1).*exp(b(2).*E_ff1.^2 +
          b(3).*E_ss1.^2 +
          b(4).*E_nn1.^2).*(b(3).*U_ss1.^2.*(U_ss1.^2 - 1) -
          b(4).*U_nn1.^2.*(U_nn1.^2-1));

% (2)

    tff_Fung2 = @(b,U)0.5.*b(1).*exp(b(2).*E_ff2.^2 +
          b(3).*E_ss2.^2 +
          b(4).*E_nn2.^2).*(b(2).*U_ff2.^2.*(U_ff2.^2 - 1) -
          b(4).*U_nn2.^2.*(U_nn2.^2-1));

    tss_Fung2 = @(b,U)0.5.*b(1).*exp(b(2).*E_ff2.^2 +
          b(3).*E_ss2.^2 +
          b(4).*E_nn2.^2).*(b(3).*U_ss2.^2.*(U_ss2.^2 - 1) -
          b(4).*U_nn2.^2.*(U_nn2.^2-1));

% Parameter Estimation

     MSE_Fung = @(b,U)(tff_Fung2(b,U) - sigma_ff2).^2 +
     (tss_Fung2(b,U) - sigma_ss2).^2;
     b0 = [1;1;1;1];
     b = lsqcurvefit(MSE_Fung,b0,U,zeros(size(sigma_ff1)));
     C = b(1); b_ff = b(2); b_ss = b(3); b_nn = b(4);

%% JCC-TMH Model

% Estimation of the Strain Energy Function from QR

    for i = 1:length(U_ff1)
        dW_da2_1(i) = (2/3)*sigma_ff1(i) - (1/3)*sigma_ss1(i);
        dW_da3_1(i) = -0.5*sigma_ss1(i);

        dW_da2_2(i) = (2/3)*sigma_ff2(i) - (1/3)*sigma_ss2(i);
```

```
        dW_da3_2(i) = -0.5*sigma_ss2(i);
    end

% Parameter Estimation from dW/da

    a = [a2_1;a3_1;a2_2;a3_2];
    % dW_da2 (1)
    Eq1_1 = @(g,a)2*g(1)*g(2).*a2_1.*exp(g(2).*a2_1.^2) + g(5);

    % dW_da3 (1)
    Eq2_1 = @(g,a)2*g(3)*g(4).*a3_1.*exp(g(4).*a3_1.^2);

    % dW_da2 (2)
    Eq1_2 = @(g,a)2*g(1)*g(2).*a2_2.*exp(g(2).*a2_2.^2) + g(5);

    % dW_da3 (2)
    Eq2_2 = @(g,a)2*g(3)*g(4).*a3_2.*exp(g(4).*a3_2.^2);

    MSE_TMH = @(g,a) (Eq1_2(g,a) - dW_da2_2).^2 + (Eq2_2(g,a) -
    dW_da3_2).^2;
    g0 = [5.209;5.737;8.8862;0.8877;-10.16];
    g = lsqcurvefit(MSE_TMH,g0,a,zeros(size(sigma_ff1)));
    af_hat = g(1); bf_hat = g(2); as_hat = g(3); bs_hat = g(4);
    c=g(5); %d=g(6);

% Predicting the Cauchy Stresses using QR (JCC-TMH)

% (1)

    tff_TMH1 = 1.5.*Eq1_1(g,a) - Eq2_1(g,a);
    tss_TMH1 = -2.*Eq2_1(g,a);

% (2)

    tff_TMH2 = 1.5.*Eq1_2(g,a) - Eq2_2(g,a);
    tss_TMH2 = -2.*Eq2_2(g,a);

% Plotting the Fits of dW/da (1)

figure (7)
    plot(dW_da2_1,'ko'); hold on; plot(Eq1_1(g,a)); axis([0 50 0
    40]);
    title('(A1) Predicted $\frac{\partial{W}}{\partial{a}_{2}}$
    from QR Model of JCC-TMH','Interpreter','latex','fontsize',12);
    xlabel('DATA POINT','fontweight','bold');
    ylabel('$\frac{\partial{W}}{\partial{a}_{2}}$','Interpreter','l
    atex','fontsize',14,'fontweight','bold');
    legend('Measured','Fit')

figure(8)
    plot(dW_da3_1,'ko'); hold on; plot(Eq2_1(g,a));
```

```
    title('(B1) Predicted $\frac{\partial{W}}{\partial{a}_{3}}$
    from QR Model of JCC-TMH','Interpreter','latex','fontsize',12);
    xlabel('DATA POINT','fontweight','bold');
    ylabel('$\frac{\partial{W}}{\partial{a}_{3}}$','Interpreter','l
    atex','fontsize',14,'fontweight','bold');
    legend('Measured','Fit')

figure(9)
    plot(a3_1,dW_da2_1,'ko'); hold on; plot(a3_1,Eq1_1(g,a),'b-');
    plot(a3_1,dW_da3_1,'k^'); hold on; plot(a3_1,Eq2_1(g,a),'r-');
    title('(C1) Dependency of $\frac{\partial{W}}{\partial{a}_{2}}$
    and $\frac{\partial{W}}{\partial{a}_{3}}$ on
    $\bf\alpha_{3}$','Interpreter','latex','fontsize',12);
    xlabel('\alpha_{3}','fontweight','bold');
    ylabel('$\frac{\partial{W}}{\partial{a}_{i}}$','Interpreter','l
    atex','fontweight','bold');
    set(legend('Measured
    $\frac{\partial{W}}{\partial{\alpha_{2}}}$','Fitted
    $\frac{\partial{W}}{\partial{\alpha_{2}}}$', 'Measured
    $\frac{\partial{W}}{\partial{\alpha_{3}}}$','Fitted
    $\frac{\partial{W}}{\partial{\alpha_{3}}}$'),'Interpreter','lat
    ex')

% Plotting the Fits of dW/da (2)

figure (10)
    plot(dW_da2_2,'ko'); hold on; plot(Eq1_2(g,a)); axis([0 50 0
    60]);
    title('(A2) Predicted $\frac{\partial{W}}{\partial{a}_{2}}$
    from QR Model of JCC-TMH','Interpreter','latex','fontsize',12);
    xlabel('DATA POINTS','fontweight','bold');
    ylabel('$\frac{\partial{W}}{\partial{a}_{2}}$','Interpreter','l
    atex','fontweight','bold');
    legend('Measured','Fit')

figure(11)
    plot(dW_da3_2,'ko'); hold on; plot(Eq2_2(g,a));
    title('(B2) Predicted $\frac{\partial{W}}{\partial{a}_{3}}$
    from QR Model of JCC-TMH','Interpreter','latex','fontsize',12);
    xlabel('DATA POINTS','fontweight','bold');
    ylabel('$\frac{\partial{W}}{\partial{a}_{3}}$','Interpreter','l
    atex','fontsize',14,'fontweight','bold');
    legend('Measured','Fit')

figure(12)
    plot(a2_2,dW_da2_2,'ko'); hold on; plot(a2_2,Eq1_2(g,a),'b-');
    plot(a2_2,dW_da3_2,'k^'); hold on; plot(a2_2,Eq2_2(g,a),'r-');
    title('(C2) Dependency of $\frac{\partial{W}}{\partial{a}_{2}}$
    and $\frac{\partial{W}}{\partial{a}_{3}}$ on
    $\bf\alpha_{2}$','Interpreter','latex','fontsize',14);
```

```
    xlabel('\alpha_{2}','fontweight','bold');
    ylabel('\bf{dW/d\alpha}','fontweight','bold');
    set(legend('Measured
    $\frac{\partial{W}}{\partial{\alpha_{2}}}$','Fitted
    $\frac{\partial{W}}{\partial{\alpha_{2}}}$', 'Measured
    $\frac{\partial{W}}{\partial{\alpha_{3}}}$','Fitted
    $\frac{\partial{W}}{\partial{\alpha_{3}}}$'),'Interpreter','lat
    ex', 'Location', 'northwest')

figure(13)
    plot(a3_2,dW_da2_2,'ko'); hold on; plot(a3_2,Eq1_2(g,a),'b-');
    plot(a3_2,dW_da3_2,'k^'); hold on; plot(a3_2,Eq2_2(g,a),'r-');
    title('(C2) Dependency of $\frac{\partial{W}}{\partial{a}_{2}}$
    and $\frac{\partial{W}}{\partial{a}_{3}}$ on
    $\bf\alpha_{3}$','Interpreter','latex','fontsize',14);
    xlabel('\alpha_{3}','fontweight','bold');
    ylabel('\bf{dW/d\alpha}','fontweight','bold');
    set(legend('Measured
    $\frac{\partial{W}}{\partial{\alpha_{2}}}$','Fitted
    $\frac{\partial{W}}{\partial{\alpha_{2}}}$', 'Measured
    $\frac{\partial{W}}{\partial{\alpha_{3}}}$','Fitted
    $\frac{\partial{W}}{\partial{\alpha_{3}}}$'),'Interpreter','lat
    ex','Location', 'northwest')
```

A.4 Quantifying the Uncertainty of Both Models

```
%% CALCULATING THE SQUARED ERROR FOR THE STRESSES FROM EACH MODEL

% Error (1)

    Err_num_Fung1 = (tff_Fung1(b,U) - sigma_ff1).^2 +
    (tss_Fung1(b,U) - sigma_ss1).^2;
    Err_num_TMH1 = (tff_TMH1 - sigma_ff1).^2 + (tss_TMH1 -
    sigma_ss1).^2;
    for i = 1:length(U_ff1)
        sigma1(:,:,i) = [sigma_ff1(i) 0 0; 0 sigma_ss1(i) 0; 0 0 0];
        Err_den1 = sum(dot(sigma1(:,:,i),sigma1(:,:,i)));
    end
   Err_Fung1 = Err_num_Fung1/Err_den1; Err_TMH1 =
   Err_num_TMH1/Err_den1;

% Error (2)

    Err_num_Fung2 = (tff_Fung2(b,U) - sigma_ff2).^2 +
    (tss_Fung2(b,U) - sigma_ss2).^2;
    Err_num_TMH2 = (tff_TMH2 - sigma_ff2).^2 + (tss_TMH2 -
    sigma_ss2).^2;
    for i = 1:length(U_ff1)
        sigma2(:,:,i) = [sigma_ff2(i) 0 0; 0 sigma_ss2(i) 0; 0 0 0];
        Err_den2 = sum(dot(sigma2(:,:,i),sigma2(:,:,i)));
    end
   Err_Fung2 = Err_num_Fung2/Err_den2; Err_TMH2 =
   Err_num_TMH2/Err_den2;
```

A.5 Plotting the Predicted Stresses from Both Models

```
%% PLOTS OF THE PREDICTED STRESSES FROM FUNG & JCC-TMH MODELS

% Plotting each of the Stresses (JCC-TMH vs Fung) and the Error in
the Total Stress

% (1)

% t_ff
figure (14)
    plot(sigma_ff1,'ko');hold on; plot(tff_Fung1(b,U),'b-'); hold
    on; plot(tff_TMH1,'r-'); hold off
    title('(A1) Predicted Fiber Cauchy Stresses (\bf\sigma_{ff})');
    xlabel('DATA POINT','fontweight','bold');
    ylabel('\bf\sigma_{ff}','fontweight','bold');legend('Data','\si
    gma_{ff} (Fung)','\sigma_{ff} (JCC-TMH)')

% t_ss
figure (15)
    plot(sigma_ss1,'k^');hold on; plot(tss_Fung1(b,U),'b-'); hold
    on; plot(tss_TMH1,'r-'); hold off
    title('(B1) Predicted Cross-fiber Cauchy Stresses
    (\bf\sigma_{ss})');
    xlabel('DATA POINT','fontweight','bold');
    ylabel('\bf\sigma_{ss}','fontweight','bold');legend('Data','\si
    gma_{ss} (Fung)','\sigma_{ss} (JCC-TMH)')

% Fiber Stress-Stretch Curve
figure (16)
    plot(U_ff1,sigma_ff1,'ko',U_ff1,tff_Fung1(b,U),'b-
    ',U_ff1,tff_TMH1,'r-'); axis([0 2 0 55])
    legend('Data','Fung Model','JCC-TMH Model'); title('(C1)
    Biaxial Fiber Stress-Stretch Data and Fitted Curves');
    xlabel('STRETCH','fontweight','bold'); ylabel('STRESS
    (g/cm^{2})','fontweight','bold');

% Cross-fiber Stress-Stretch Curve
figure (17)
    plot(U_ss1,sigma_ss1,'k^',U_ss1,tss_Fung1(b,U),'b-
    ',U_ss1,tss_TMH1,'r-')
    legend('Data','Fung Model','JCC-TMH QR Model'); title('(D1)
    Biaxial Cross-fiber Stress-Stretch Data and Fitted Curves');
    xlabel('STRETCH','fontweight','bold'); ylabel('STRESS
    (g/cm^{2})','fontweight','bold');
```

```
% (2)

% t_ff
figure (18)
    plot(sigma_ff2,'ko');hold on; plot(tff_Fung2(b,U),'b-'); hold
    on; plot(tff_TMH2,'r-'); axis([0 25 0 110]); hold off
    title('(A2) Predicted Fiber Cauchy Stresses (\bf\sigma_{ff})');
    xlabel('DATA POINT','fontweight','bold');
    ylabel('\bf\sigma_{ff}
    (g/cm^{2})','fontweight','bold');legend('Data','\sigma_{ff}
    (Fung)','\sigma_{ff} (JCC-TMH)')

% t_ss
figure (19)
    plot(sigma_ss2,'k^');hold on; plot(tss_Fung2(b,U),'b-'); hold
    on; plot(tss_TMH2,'r-'); hold off
    title('(B2) Predicted Cross-fiber Cauchy Stresses
    (\bf\sigma_{ss})');
    xlabel('DATA POINT','fontweight','bold');
    ylabel('\bf\sigma_{ss} (g/cm^{2})','fontweight','bold');
    legend('Data','\sigma_{ss} (Fung)','\sigma_{ss} (JCC-TMH)')

% Fiber Stress-Stretch Curve
figure (20)
    plot(U_ff2,sigma_ff2,'ko',U_ff2,tff_Fung2(b,U),'b-
    ',U_ff2,tff_TMH2,'r-')
    legend('Data','Fung Model','JCC-TMH Model'); title('(C2)
    Biaxial Fiber Stress-Stretch Data and Fitted Curves');
    xlabel('STRETCH','fontweight','bold'); ylabel('STRESS
    (g/cm^{2})','fontweight','bold');

% Cross-fiber Stress-Stretch Curve
figure (21)
    plot(U_ss2,sigma_ss2,'k^',U_ss2,tss_Fung2(b,U),'b-
    ',U_ss2,tss_TMH2,'r-')
    legend('Data','Fung Model','JCC-TMH Model'); title('(D2)
    Biaxial Cross-fiber Stress-Stretch Data and Fitted Curves');
    xlabel('STRETCH','fontweight','bold');
    ylabel('STRESS (g/cm^{2})','fontweight','bold');

%% PLOTTING THE SQUARED ERROR OF EACH MODEL

% t_error (2)
figure (22)
    plot(Err_Fung2,'b-'); hold on; plot(Err_TMH2,'r-')
    title('(E2) The Uncertainty in \bf{\sigma_{Fung}} &
    \bf{\sigma_{JCC-TMH}}');
    xlabel('DATA POINT','fontweight','bold');
    ylabel('\bf\sigma_{error}','fontweight','bold');
    legend('Err(Fung)','Err(JCC-TMH)')
```

APPENDIX B

MATLAB CURVE FITTING TOOL PLOTS

Using the MATLAB curve fitting tool, the resulting material constants from the second data set were used to plot the functional forms of both $\partial W/\partial \alpha_2$ and $\partial W/\partial \alpha_3$, and the goodness of fit was evaluated using the statistical parameters shown in **Table B-1**.

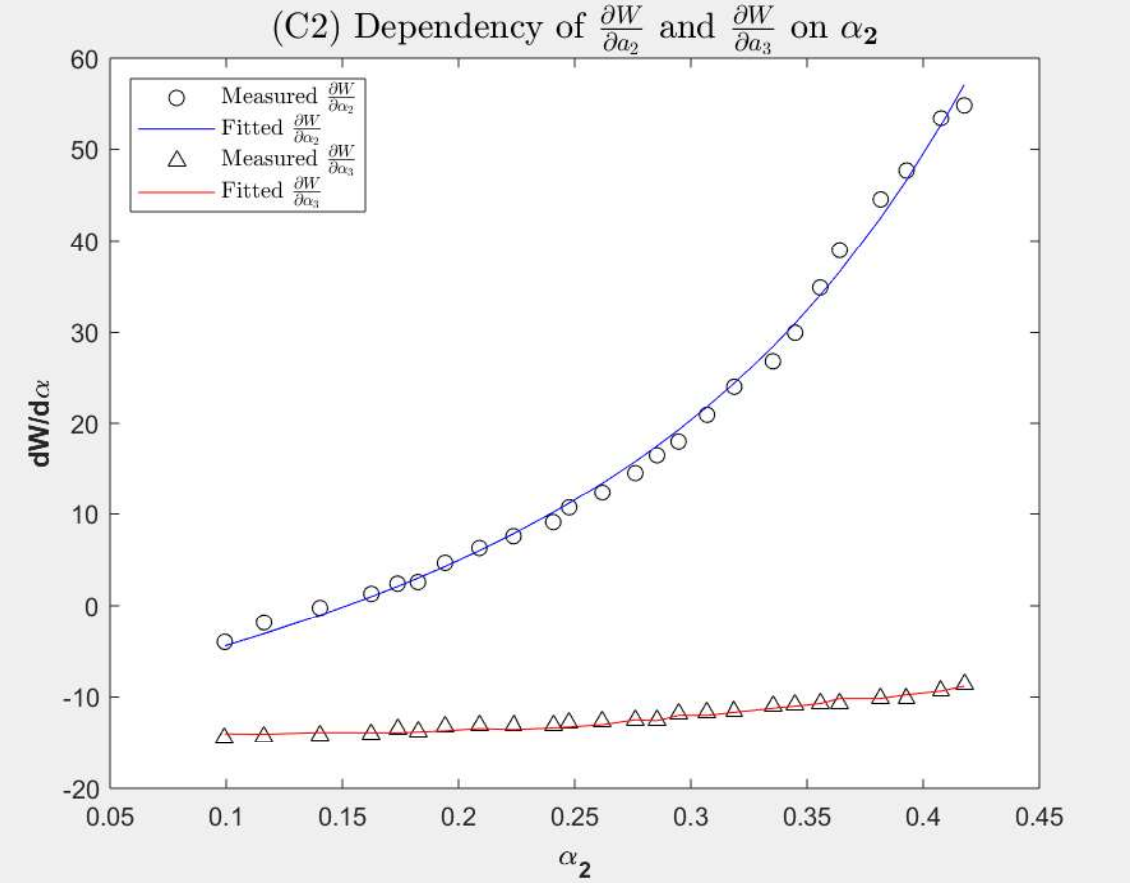

Figure B-1. Plotting α_2 against $\partial W/\partial \alpha$, where the circles and triangles represent the experimental data of $\partial W/\partial \alpha_2$ and $\partial W/\partial \alpha_3$, respectively, and the blue curve and the red curve represent the fitted $\partial W/\partial \alpha_2$ and $\partial W/\partial \alpha_3$, respectively.

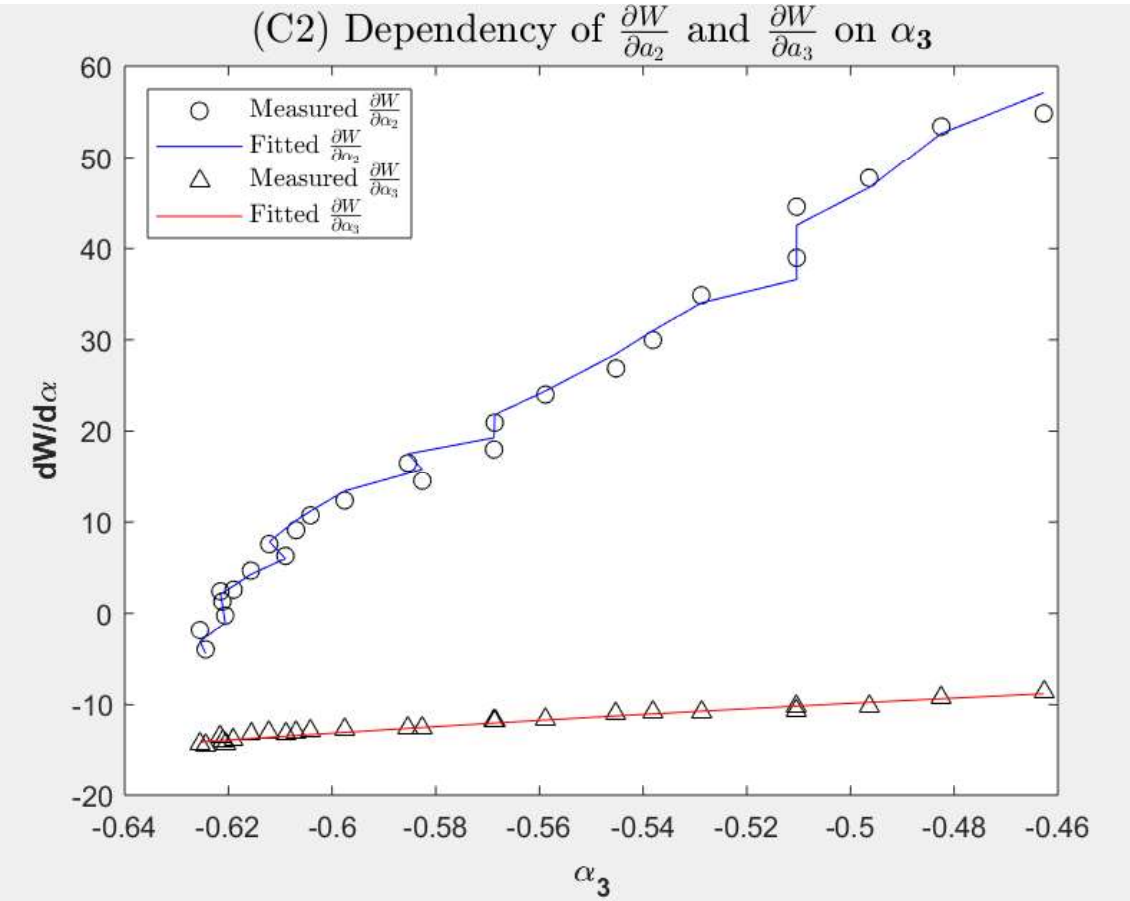

Figure B-2. Plotting α_3 against $\partial W/\partial \alpha$, where the circles and triangles represent the experimental data of $\partial W/\partial \alpha_2$ and $\partial W/\partial \alpha_3$, respectively, and the blue curve and the red curve represent the fitted $\partial W/\partial \alpha_2$ and $\partial W/\partial \alpha_3$, respectively.

Table B-1. Goodness of fit statistics for the fitted $\partial W/\partial \alpha_i$ with respect to α_2 and α_3

	SSE	***R-square***	***Adjusted R-square***	***RMSE***
$\partial W/\partial \alpha_2$ vs. α_2	28.3	0.996	0.996	1.13
$\partial W/\partial \alpha_3$ vs. α_3	10.1	0.993	0.993	0.664

The statistical parameters shown in **Table B-1** are the sum of squares due to error (SSE), r-square, adjusted r-square, and the root mean squared error (RMSE).